Microglia undergo rapid phenotypic transformation in acute brain slices but remain essential for neuronal synchrony

Short title: Microglial support of neuronal activity in acute slices

Péter Berki[1,7,8¶], Csaba Cserép[2¶], Balázs Pósfai[1,2], Eszter Szabadits[2], Zsuzsanna Környei[2], Anna Kellermayer[2], Miklós Nyerges[2], Xiaofei Wei[3], Istvan Mody[3], Kunihiko Araki[4], Heinz Beck[4], Kaikai He[5], Ya Wang[6], Zhaofa Wu[5], Miao Jing[6], Yulong Li[5], Attila I. Gulyás[7] and Ádám Dénes[2,*]

[1] János Szentágothai Doctoral School of Neuroscience, Semmelweis University, Budapest, H-1083 Hungary

[2] Momentum Laboratory of Neuroimmunology, Institute of Experimental Medicine, Budapest, H-1083 Hungary

[3] Department of Neurology, The David Geffen School of Medicine at UCLA, Los Angeles, CA 90095 USA

[4] Institute of Experimental Epileptology and Cognition Research, Medical University of Bonn, Bonn, 53127 Germany

[5] State Key Laboratory of Membrane Biology, New Cornerstone Science Laboratory, School of Life Sciences, Peking University, Beijing 100871, China

[6] Chinese Institute for Brain Research, Beijing 102206, China

[7] Laboratory of Cerebral Cortex Research, Institute of Experimental Medicine, Budapest, H-1083 Hungary

[8] Laboratory of Neuronal Network and Behaviour, Institute of Experimental Medicine, Budapest, H-1083 Hungary

[*]Corresponding author
E-mail: denes.adam@koki.hu

[¶]These authors share first authorship on this work.

Abstract

Acute brain slices represent a "workhorse" model for studying the central nervous system (CNS) from nanoscale events to complex circuits. While slice preparation inherently involves tissue injury, it is unclear how microglia, the main immune cells and damage sensors of the CNS shape tissue integrity *ex vivo*. To this end, we have studied the mechanisms of microglial phenotype changes and contribution to neuronal network organisation and functioning in acute brain slices. Using a novel ATP-reporter mouse line and microglia reporter mice, we show that acute slice preparation induces rapid, P2Y12 receptor (P2Y12R) dependent dislocation and migration of microglia, paralleled with marked

morphological transformations driven by early ATP surges and subsequent ATP flashes. Gradual depolarization of microglia is associated with the downregulation of purinergic P2Y12R and time-dependent changes of microglia-neuron interactions, paralleled by altered numbers of excitatory and inhibitory synapses. Importantly, functional microglia not only modulate synapse sprouting, but the absence of microglia or microglial P2Y12R markedly diminishes the incidence, amplitude, and frequency of sharp wave-ripple activity in hippocampal slices. Collectively, our data suggest that microglia are inherent modulators of complex neuronal networks, and their specific actions are indispensable to maintain neuronal network integrity and activity *ex vivo*. These findings could facilitate new lines of research resulting in improved *ex vivo* methodologies and a better understanding of microglia-neuron interactions both in physiological and pathological conditions.

Introduction

Since its first applications several decades ago (Andersen, 1981; Yamamoto & McIlwain, 1966), the acute brain slice preparation technique has become a key tool in the field of neuroscience and has extensively contributed to our understanding of cellular physiology. As the methodology of slice preparation went through numerous iterations over the years (Brahma et al., 2000; Richerson & Messer, 1995; Ting et al., 2014), improvements have led to acute slices even capable of producing spontaneous oscillations, similar to those observed *in vivo* (Hájos et al., 2013; Mann et al., 2005; Perumal et al., 2021; C. Wu et al., 2005). Meanwhile, *ex vivo* studies of non-neuronal cell types such as astrocytes and microglia have also been emerging (Kettenmann et al., 2011; Verkhratsky & Nedergaard, 2018), alongside with increasing focus on bidirectional communication between neurons and glial cells (Eyo & Wu, 2013; Pannasch & Rouach, 2013). Microglia are the primary immune cells of the CNS parenchyma, with essential roles beyond their immune function under both physiological and pathological conditions (Masuda et al., 2020; Prinz et al., 2019). Because microglia are heavily involved in brain development and maintenance of neuronal populations (Kierdorf & Prinz, 2017; Thion et al., 2018), while their functional alterations are linked to a wide range of human diseases (Salter & Stevens, 2017; Song & Colonna, 2018; Wang & Colonna, 2019), interest in understanding microglial

function has substantially increased over the last decade. As such, acute slice preparations also proved to be an essential tool for the investigation of microglia, with better preservation of microglial phenotype resembling their physiological states than the *in vitro* culture system (Bennett et al., 2018; Bohlen et al., 2017; Butovsky et al., 2014; Gosselin et al., 2017; Izquierdo et al., 2019), based on robust transcriptomic, proteomic and functional evidence (Boucsein et al., 2000, 2003; Butovsky et al., 2014; Färber & Kettenmann, 2005; Hellwig et al., 2013; Kettenmann et al., 2011; Melief et al., 2012; Schilling & Eder, 2007a; Schmid et al., 2009). However, it is also acknowledged that microglia can become reactive in slices and transform to an amoeboid phenotype (Haynes et al., 2006; Petersen & Dailey, 2004; Stence et al., 2001). Importantly, while the acute slice technique has contributed to understand microglial physiology (Boucsein et al., 2000; Färber & Kettenmann, 2005; Kettenmann et al., 2011; Schilling et al., 2000; Schilling & Eder, 2007b), the impact of methodological practices, relevant time frames, mechanisms influencing microglial states upon slice preparation, and most importantly, the impact of microglial function on electrophysiological measurements have remained vaguely characterized. Despite the known sensitivity of microglia to even subtle changes in their microenvironment (Hirbec et al., 2019; Masuda et al., 2020) mechanistic data from the first few minutes to hours after slice preparation (a relevant time frame for most studies) with appropriate temporal resolution to assess microglial states are not available at present. Thus, it is currently unclear how time-dependent changes of microglia may influence complex neuronal circuits and their reorganization in acute slice preparation. To this end, we set out to investigate microglial phenotype changes and their impact on neuronal networks simultaneously, in slice preparations capable of producing spontaneous network activity by using an experimentally relevant timeframe. For these studies, we made use of established protocols and the extensive expertise in slice preparation available at three independent research laboratories which pioneered the preparation of high quality brain slices and introduced technical developments enabling the first investigation of complex network oscillations (Ferando & Mody, 2015; Hájos et al., 2009; Hájos & Mody, 2009; Remy et al., 2003). Our results suggest that microglia maintain fundamental features of neuronal networks in acute slice preparations, which is remarkably influenced by microglial phenotype changes due to slice preparation-evoked, acute- and

sustained ATP release. These observations may be of importance for virtually all acute brain slice studies investigating either neuronal function or microglial responses.

Results

Microglia gradually migrate towards the surface of acute slice preparations

Microglia are well known to react rapidly to injury or tissue disturbance in the brain parenchyma (Davalos et al., 2005; Nimmerjahn et al., 2005). To investigate how injury caused by acute slice preparation influences microglial functions at population level, we first tracked microglial cell body and process distribution during a 5-hours incubation in 300 µm thick acute hippocampal slices from CX3CR1$^{+/GFP}$ microglia reporter mice (p.n.:~35 days). We used a strictly controlled preparation and incubation procedure across all measurements (see details in Methods), optimized for studying spontaneously occurring sharp wave-ripple activity (SWR) (Hájos et al., 2013; Schlingloff et al., 2014). To monitor time dependent changes, slices were immersion-fixed at different timepoints after cutting (Fig 1A). Subsequently, preparations were re-sectioned and mounted onto glass plates for analysis (Fig 1B). Only the native microglial GFP signal was imaged via confocal laser-scanning microscopy (Fig 1C). We found that translocation of microglial cell bodies occurs rapidly after slice preparation with most extensive changes in the top region (~40 µm) of slices (Fig 1D). Here, the density of cell bodies gradually increased by 75% throughout the 5 hours of the incubation (Mann-Whitney, $p<0.01$), and reached significance at 42% ($p<0.05$) as early as 2 hours of incubation (Fig 1E; blue). Top region of slices showed a 42% higher density of cell bodies when compared to the bottom region (Mann-Whitney, $p<0.01$) after 2 hours of incubation, a relevant timepoint for most electrophysiological measurements (ref, Fig 1E, black statistical indication). We calculated the lowest distance of required cell displacement to reach the 5 hours distribution starting from the 0-minute distribution (Fig 1F). Our results show that the translocation of cell bodies is a composite of two effects: a stronger effect acting in the direction of the top surface and a smaller effect acting towards the top and bottom cut surfaces away from the middle of the slices. The total number of microglia located in whole cross sections did not differ significantly

during the experiment (43.07 cells/grid at 0 min, 41.50 cells/grid at 5 hours; $p=0.788$), suggesting that microglia loss does not contribute to the observed changes in cell distribution.

In line with this, the spatial distribution of microglial processes within the slice showed similar, but even more pronounced alterations during the incubation process (Fig 1G). Microglial process density in the top layer increased significantly by 21% ($p<0.05$) as early as 2 hours of incubation and by 29% ($p<0.001$) after 5 hours of incubation (Fig 1H, blue). Contrary to microglial cell bodies, process density at the bottom layer showed a significant drop by 15% ($p<0.05$) already after 2 hours of incubation (Fig 1H, green). Here, we also observed 23% ($p<0.05$) lower process density at the bottom region of slices compared to top after 5 hours of incubation (Fig 1H; black statistical indication, independent t-test). Importantly, the total percentage of area covered by microglial processes dropped to half between the 0-minute (acute slices fixed immediately after cutting) and 5-hour timepoints ($p<0.0001$, independent t-test, Fig 1I).

To capture these changes in real time, slice preparations were transferred into a recording chamber for confocal imaging (Fig 1J). The native signal of microglia (CX3CR1$^{+/GFP}$) was continuously imaged for at least 6 hours after slice preparation (Fig 1K, Supplementary Video 1-2). We found that individual cell behaviours correlated with the quantitative measurements above (Fig 1E-F, H-I), with both processes and the cell body of microglia (Fig 1K, coloured dots) expressing directed movement towards the top surface of slices (Fig 1K, white dashed line).

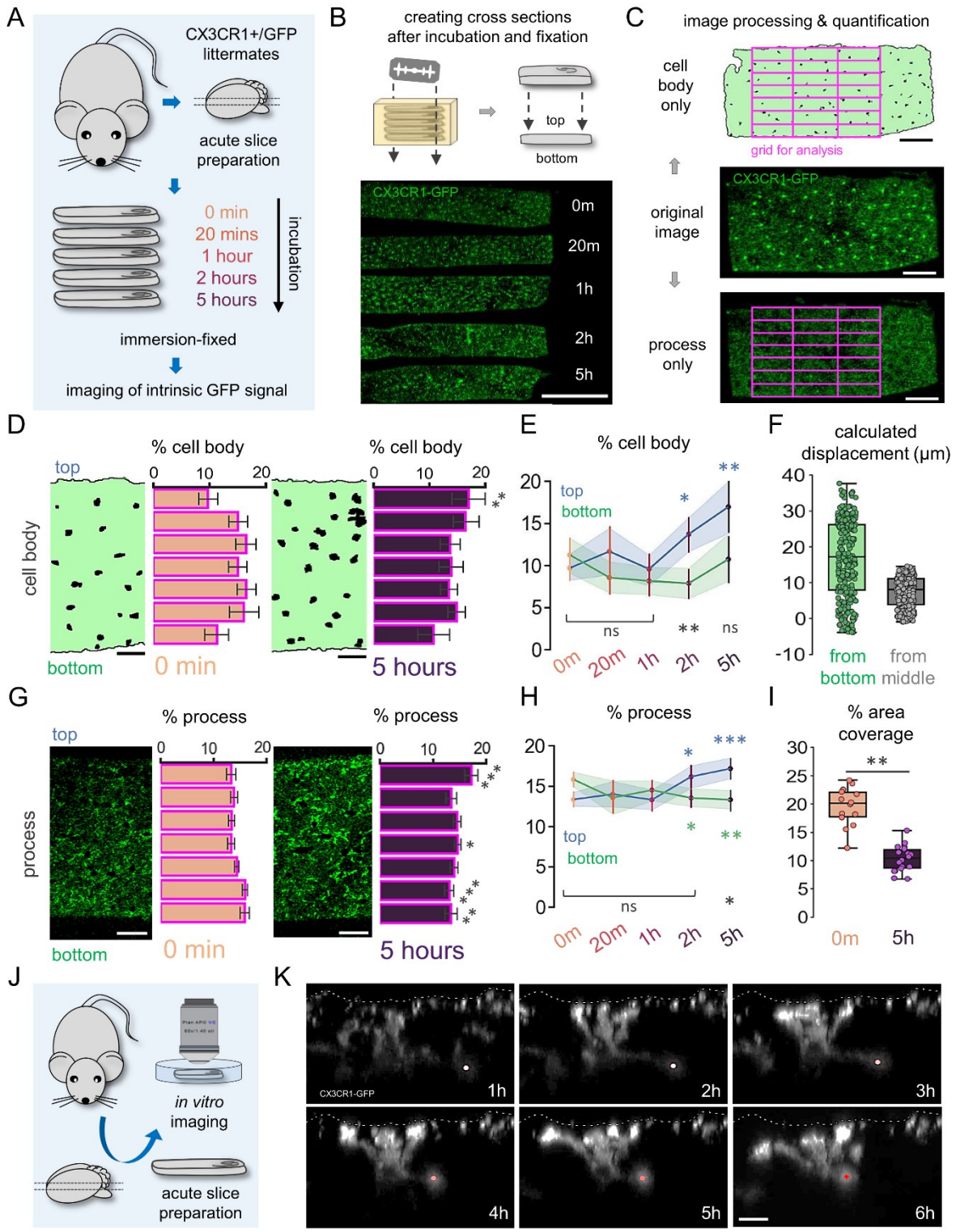

Figure 1. Microglia gradually migrate towards the surface of acute slice preparations

A. Schematic representation of the experiment. CX3CR1$^{+/GFP}$ littermates (N=3; p.n.: ~35 days) were used to create acute hippocampal slice preparations and placed into an interface-type incubation chamber for recovery. Slices were immersion-fixed immediately (0 minute) or after 20 minutes, 1 hour, 2 hours or 5-hours of incubation.

B. Cross sections were made from slice preparations that were fixed at different timepoints (top). Maximum intensity projection image shows cross-sections of slices mounted onto glass plates while preserving their

top and bottom directionality according to their position in the incubation chamber. Native GFP signal of microglia were imaged via confocal laser-scanning microscopy (bottom, bar: 500 µm).

C. Original images were further processed (to contain either cell bodies or processes) and a 7x3 grid (violet) was used consequently for the quantification of cell body or process distributions along the grid layers (bar: 100 µm).

D. Representative sections of processed images at 0 minute and 5 hours showing distribution of microglial cell bodies along the top and bottom axis of slices (left, bar: 50 µm). Bar-plots are showing percentages of total cell bodies counted respective to the layers of the analysis grid (right). N=3, 3 slices/animal, mean ± SEM, independent t-test, **: $p<0.01$.

E. Line-plots representing measured changes of microglial cell body percentages across different timepoints within the top (blue) and bottom (green) layers of acute slice preparations. N=3, 3 slices/animal, median ± SEM, Mann-Whitney, ns: not significant, *: $p<0.05$, **: $p<0.01$. Blue statistical indications show significant changes compared to 0-minute timepoint, black statistical indications compare top and bottom means at each timepoint.

F. Cell body translocation quantified as minimum required displacement (µm) towards the top measured from bottom (green) or middle (grey). N=3, p.n.: ~35 days; 3 slices/animal.

G. Same as in D) respective to microglial process fluorescence intensity calculated for each layer in the grid, mean ± SEM, Mann-Whitney, **: $p<0.01$.

H. Same as in E) respective to microglial process fluorescence intensity. N=3, p.n.: ~35 days; 3 slices/animal; mean ± SEM, independent t-test, ns: not significant, *: $p<0.05$, **: $p<0.01$, ***: $p<0.001$.

I. Percent of area covered by processes at the 0-minute and 5-hours timepoints, Mann-Whitney, **: $p<0.01$.

J. $CX3CR1^{+/GFP}$ mice (p.n.:45-80 days) were used to create acute hippocampal slices and transferred into a recording chamber for confocal or 2P imaging after cutting.

K. Extracted timeframes from Supplementary Video 1. Images show the translocation of microglial processes and the cell body towards the surface of slice preparations (white stripped line). Scale bar: 10 µm.

Microglia undergo rapid, progressive morphological changes in acute slices

Microglial cells are well known to extend their processes towards injury as an early response, followed by marked morphological transformation (Haynes et al., 2006; Petersen & Dailey, 2004; Stence et al., 2001). Decrease in the area covered by microglial processes (Fig 1I) suggested robust changes in microglia morphology taking place in acute slice preparations. This behaviour was also evident in the data gathered by our imaging experiments, where we saw rapid morphological transformation of individual microglial cells (Fig 2A, Supplementary Video 3). To define the spatio-temporal characteristics of these pronounced morphological changes, preparations were immersion-fixed at different timepoints during incubation. In parallel, a group of mice were transcardially perfused to obtain slice preparations from the same brain area as controls (Fig 2B). Confocal images were analysed using unbiased automated morphological analysis (Fig 2C; Heindl et al., 2018).

Slice preparation induced drastic morphological differences in microglia. We observed rapid retraction of processes already visible in maximum intensity projection images created from the analysed z-stacks (Fig 2D), as well as on individual cell morphologies and skeleton reconstructions via the analysis tool (Fig 2E; Supplementary Video 4). Sphericity values of individual cells (amoeboid shape and retraction of processes translate to higher sphericity values) increased by ~50% on average already after 20 minutes of incubation (independent t-test, $p<0.0001$), and peaked at ~100% increase ($p<0.0001$) between 1 and 2 hours of incubation both in regions of the cortex and in the hippocampus (Fig 2F). At the same time, total number of process endings dropped by ~50% after 20 minutes of incubation ($p<0.0001$), and this reduction also peaked between 1- and 2 hours of incubation with ~80% decrease in average (Fig 2G, $p<0.0001$). We also conducted this experiment in an older group of animals (p.n.: ~95) and observed the same extensive changes concerning both cortical and hippocampal regions (Supplementary Fig 1). Based on these observations, we concluded that microglia showed rapid morphological changes in acute slice preparations.

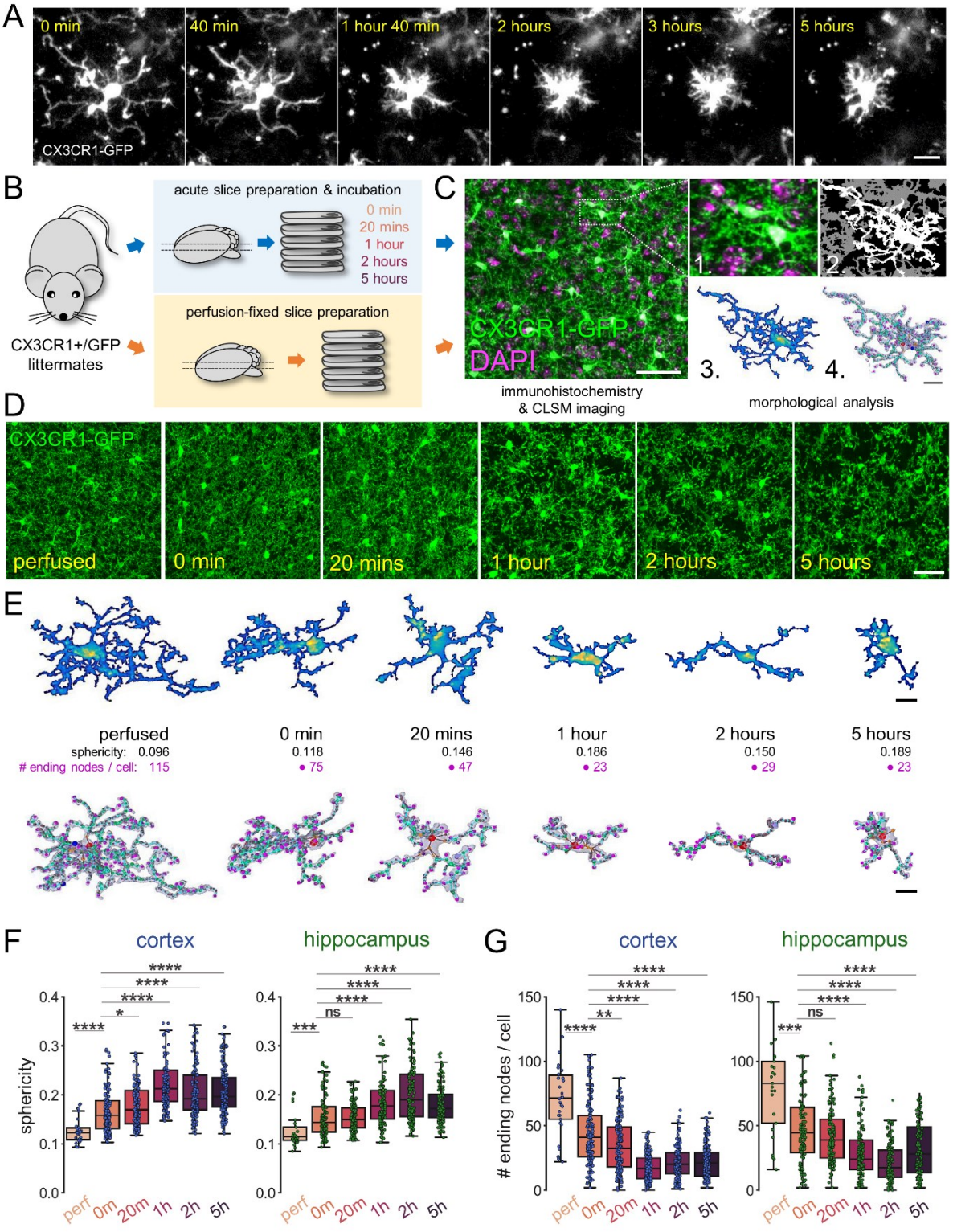

Figure 2. Microglia undergo rapid, progressive morphological changes in acute slices

A. Extracted timeframes from Supplementary Video 3. CX3CR1$^{+/GFP}$ signal of a single microglial cell was captured via confocal imaging at different timepoints after acute slice preparation. Scale bar: 10 µm.

B. Schematic representation of experiment. CX3CR1$^{+/GFP}$ littermates (N=8; p.n.: ~35 days) were used either to create hippocampal slice preparations, which were immersion-fixed before (0 minute) and after 20 minutes,

1 hour, 2 hours, or 5 hours of incubation (blue arrows), or animals were perfusion fixed to obtain slice preparations with the same dimensions as acute slices (red arrows).

C. Slices were stained and z-stack images were obtained via confocal laser-scanning microscopy (left, bar: 20 µm). Images were analysed with an automated morphological analysis tool (Heindl et al, 2018) which uses raw z-stacks (1.) to isolate and segment the images to separate microglial cells (2.). Separate cells are further segmented (3.) to cell body (yellow) and processes (blue, purple). Finally, a skeleton is constructed (4.) representing a 3D-model of each individual microglial cell (right, bar: 10 µm).

D. Maximum intensity projections of analysed confocal images showing microglial cells in perfused or immersion-fixed slices (bar: 50 µm).

E. Top row: individual microglial cells at each timepoint respective to section C) above (yellow: cell body; blue, purple: processes; bar: 5 µm). Bottom row: reconstructed skeletons for each cell depicted in middle row, together with their sphericity values (black) and total number of process endings (violet, cell body: red dot, bar: 5 µm).

F. Quantification of extracted morphological features regarding sphericity in cortex (green) and in hippocampus (pink). N=8 animal, p.n.: ~35 days; Mann-Whitney, ns: not significant, *: p<0.05, **: p<0.01, ***: p<0.001, ****: p<0.0001.

G. Same as in E) regarding number of process endings / cell in cortex (green) and in hippocampus (pink). N=8 animal, p.n.: ~35 days; Mann-Whitney, ns: not significant, *: p<0.05, **: p<0.01, ***: p<0.001, ****: p<0.0001.

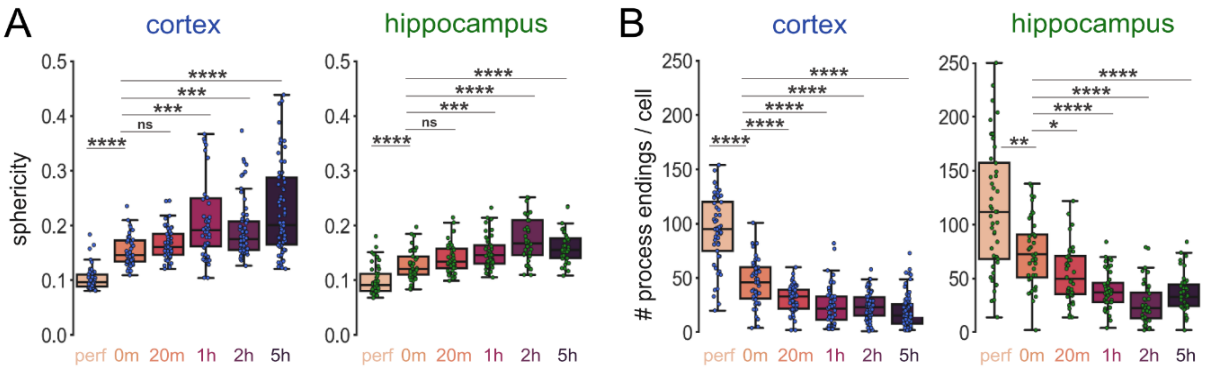

Supplementary Fig 1: Morphological changes of microglia in acute slice preparations obtained from an older group of mice (p.n.: ~95 days)

A. Quantification of extracted morphological features regarding sphericity in cortex (green) and in hippocampus (pink). CX3CR1$^{+/GFP}$ littermates, N=5 animal, p.n.: ~95 days; Mann-Whitney, ns: not significant, *: p<0.05, **: p<0.01, ***: p<0.001, ****: p<0.0001.

B. Same as in A) regarding number of process endings / cell in cortex (green) and in hippocampus (pink). N=5 animal, p.n.: ~95 days; Mann-Whitney, ns: not significant, *: p<0.05, **: p<0.01, ***: p<0.001, ****: p<0.0001.

Migration and rapid phenotype changes of microglia during the incubation process do not depend on cutting techniques

To investigate whether different slice cutting techniques could influence the extent or temporal course of microglial phenotype changes during the incubation process, we next compared acute slice samples across three independent laboratories (Lab #1, Lab #2, Lab #3) using identical fixation protocol and timing for serial preparations, but left native, well-established slice cutting techniques intact by each laboratory. Briefly: Lab#1 used an ice-cold, sucrose-based cutting solution, and slices were incubated in an interface-type chamber filled with carbonated standard ACSF. Lab #2 used an ice-cold, N-methyl-D-glucamine (NMDG)-based cutting solution, and slices were incubated in a low Na^+, sucrose-based ACSF while floating in a Styrofoam "boat" with a netting at the bottom on the surface of an incubation chamber; Lab #3 used an ice-cold, sucrose-based ACSF solution, and slices were incubated in a storage chamber filled with carbonated standard ACSF (for details see: Methods). Of note, we also tested slice preparation using a room-temperature cutting solution, which did not alter the course of microglial changes (data not shown). In all laboratories, slices were immersion-fixed in 4% PFA. Then, histological processing, imaging and analysis were performed in a uniform and blinded manner at the IEM (Fig 3A-C). Confirming our earlier results, both the sphericity of microglial cells (Fig 3D) and the number of ending nodes (Fig 3E) showed closely identical changes, similarly to microglial cell body migration and process movements (Fig 3F) suggesting that the observed changes are general, common characteristics of different acute slice preparation techniques.

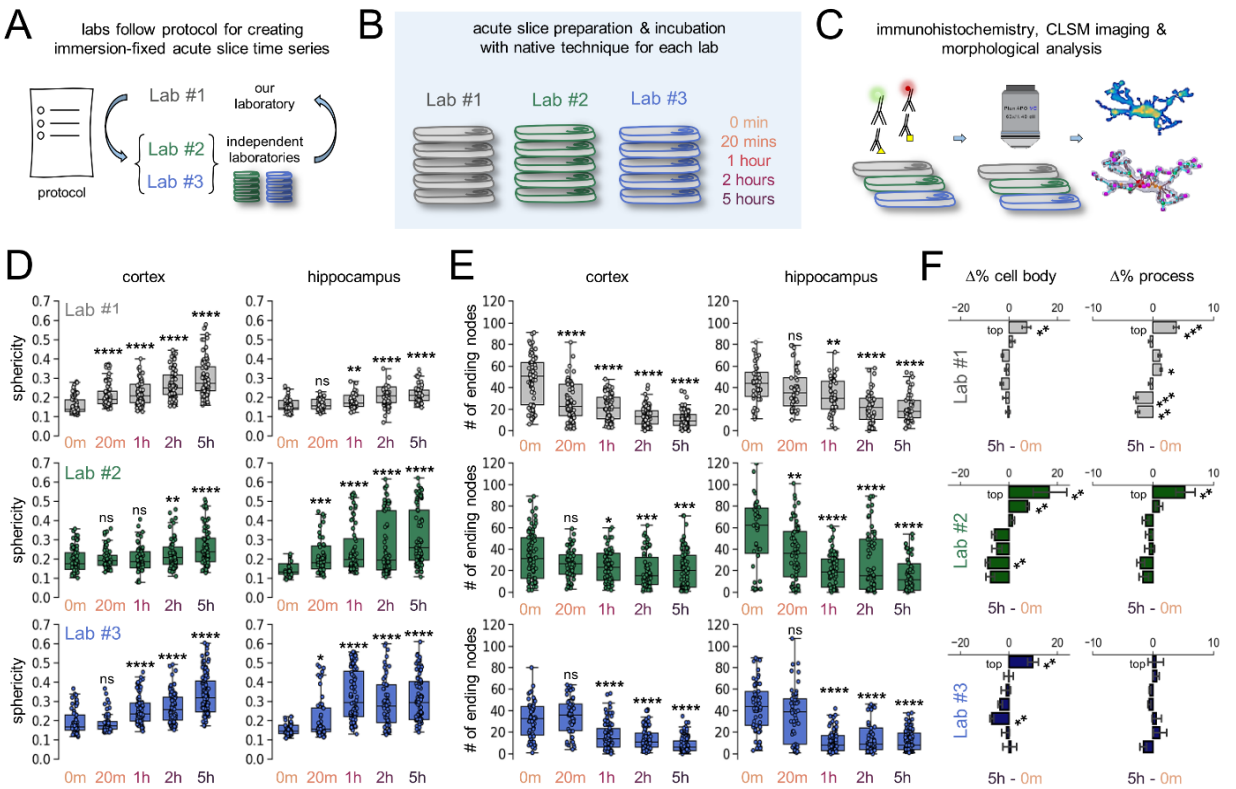

Figure 3. Migration and rapid phenotype changes of microglia during the incubation process do not depend on cutting techniques

A. Schematic representation of experiment. To compare different laboratories and acute slice preparation techniques, two independent laboratories received a protocol to synchronize acute slice fixation timepoints and fixation methods.

B. Independent laboratories were using their own native acute slice preparation method to harvest and fixate slices at specific timepoints according to the protocol.

C. Acute slice preparations were sent to our laboratory after fixation and preparation for transport (see: Methods), where they were treated together during immunostaining, imaging, and morphological analysis.

D. Quantification of extracted morphological features across different laboratories regarding sphericity in cortex (left) and in hippocampus (right). N=2 animal/lab, p.n.: ~65 days; Mann-Whitney, ns: not significant, *: p<0.05, **: p<0.01, ***: p<0.001, ****: p<0.0001.

E. Same as in D, regarding number of ending nodes/cell in cortex (left) and in hippocampus (right). N=2 animal/lab, p.n.: ~65 days; Mann-Whitney, ns: not significant, *: p<0.05, **: p<0.01, ***: p<0.001, ****: p<0.0001.

F. Bar plots representing measured changes of microglial cell body numbers (left) and area covered by processes (right) in percentages calculated between 0 min and 5 hours across the top and bottom layers of acute slice preparations. N=2 animal/lab, median ± SEM, Mann-Whitney, ns: not significant, *: p<0.05, **: p<0.01, ***: p<0.001.

Rapid downregulation of P2Y12R is accompanied by gradual microglial depolarization during the incubation process

To further investigate the extent of microglia transformation during the incubation process, we next examined changes in microglial P2Y12 receptor (P2Y12R) levels, a core microglial receptor through which microglia sense and influence neuronal activity and fate (Cserép et al., 2020; Dissing-Olesen et al., 2014; Eyo et al., 2014; Gu et al., 2016; Kato et al., 2016), and which is downregulated upon injury and inflammatory challenges (Haynes et al., 2006; Mildner et al., 2017). Pre-embedding immunofluorescent labelling indicated a marked reduction of P2Y12R labelling intensity already 1 hour after slice preparation (Fig 4A). To quantitatively examine these changes during the whole incubation process, acute slice preparations were immersion-fixed at different timepoints during incubation (Fig 4B), followed by visualization of P2Y12R with a recently developed quantitative post-embedding immunofluorescent labelling technique (Holderith et al., 2020), enabling unbiased assessment of P2Y12R labelling intensity changes (Fig 4C). We quantified P2Y12R labelling intensity at microglial cell bodies (Fig 4D, left), thick processes (Fig 4D, middle) and thin processes (Fig 4D, right), to investigate whether different subcellular compartments are differentially affected. Confirming our immunofluorescent results, we found a consistent, rapid decrease in P2Y12R labelling intensity in all the compartments until 1 hour of incubation, followed by a slight increase towards the 5-hour timepoint (Fig 4E). Loss of P2Y12R was most prominent in thick and thin processes (Fig 4E, middle, right), and less apparent on microglial cell bodies (Fig 4E, left). As such, already after 1 hour of incubation, the labelling intensity of P2Y12R (arbitrary unit, see: Methods) dropped by 25% on thick processes ($p<0.01$), 29% on thin processes ($p<0.001$) and 20% ($p<0.05$) at cell bodies of microglia.

Microglial phenotype changes have been shown to correlate with resting membrane potential, while the tonically active K^+ channels responsible for maintaining resting membrane potential are known to be potentiated by P2Y12R actions (Madry, Kyrargyri, et al., 2018; Swiatkowski et al., 2016), especially in response to injury when exposure to high ATP/ADP levels. Therefore, rapid P2Y12R downregulation is expected to be accompanied with membrane depolarization. To test this, we performed electrophysiological recordings from microglia in acute slices. As in previous experiments, acute slice preparations were placed into an interface type incubation chamber for recovery and then

263 transferred to a recording chamber at different timepoints during incubation, to measure microglia in
264 whole cell patch-clamp configuration. Targeting of microglial cells was guided by the intrinsic GFP
265 signal across the hippocampal CA1-CA3 stratum lacunosum-moleculare and stratum radiatum regions,
266 and below ~40 µm measured from the slice surface (Fig 4F). Our results showed that microglial cells
267 became gradually more depolarized throughout the total 5 hours of the incubation process (Fig 4G, left;
268 N=158 cells measured in slices from a total of 10 animals), while we did not observe significant changes
269 in input resistance (Fig 4G, right). Taken together, microglia undergo rapid phenotype changes in acute
270 slice preparations, as characterized by cell body and process translocation (Fig 1, 3), quick
271 morphological shift towards a reactive shape (Fig 2, 3), as well as early P2Y12R downregulation and
272 gradual depolarization of resting membrane potential (Fig 4).

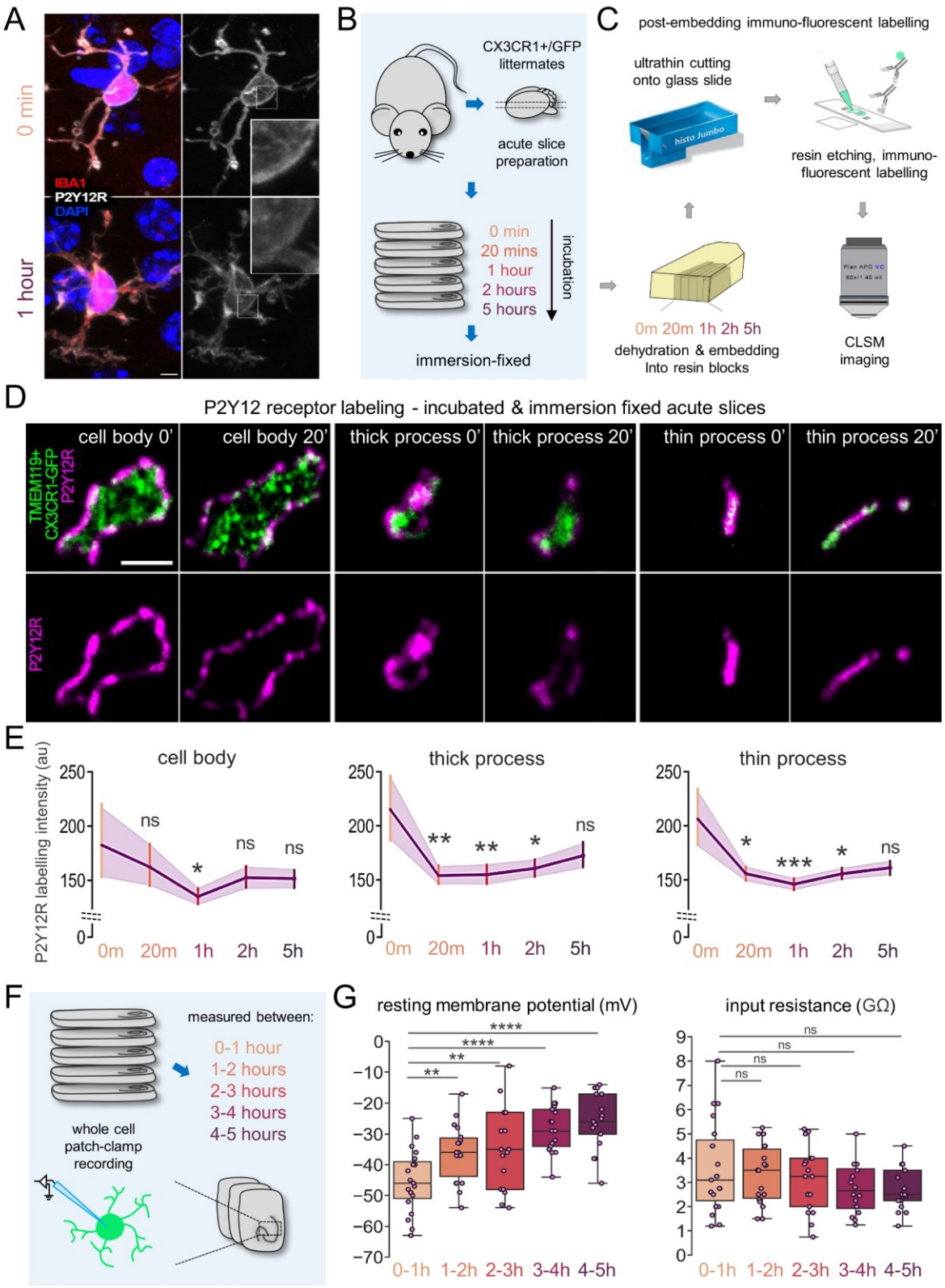

Figure 4. Rapid downregulation of P2Y12R is accompanied by gradual depolarization of microglia during the incubation process

A. Single image planes of multi-channel confocal laser scanning microscopy z-stacks, depicting microglial cells with pre-embedding immunofluorescent labelling (IBA1, red; P2Y12 receptors, white) before (0 min) and after 1 hour of incubation (bar: 3 µm).

B. Schematic representation of the experiment. CX3CR1$^{+/GFP}$ littermates (N=3; p.n.: ~35 days) were used to create acute hippocampal slice preparations and placed into an interface-type incubation chamber for recovery. Slices were immersion-fixed before (0 minute) or after 20 minutes, 1 hour, 2 hours, and 5 hours of incubation.

C. After fixation, P2Y12 receptor labelling was performed by a post-embedding immunofluorescent labelling technique: slices were dehydrated and embedded into resin blocks. Subsequently, ultrathin slices were cut onto glass slides and labelled after resin etching. Finally, z-stack images were gathered from preparations via high-resolution confocal laser scanning microscopy.

D. Representative images of P2Y12 receptor labelling via the post-embedding technique. Microglial cell bodies (left), thick processes (middle) and thin processes (right) are shown together with the P2Y12R labelling (top row) and P2Y12R labelling only (bottom row) at 0- and 20-minute timepoints (Scale bar: 2 µm).

E. Quantification of P2Y12 receptor labelling intensity (arbitrary unit, see: Methods) in microglial cell body (left), thick processes (middle) and thin processes (right.) N=3 animal, p.n.: 35 days; 3 slices/animal; Mann-Whitney, ns: not significant, *: $p<0.05$, **: $p<0.01$, ***: $p<0.001$.

F. Schematic representation of the experiment. CX3CR1$^{+/GFP}$ littermates (N=10, p.n.: ~95 days) were used to create acute slices. Microglial cells were measured in whole cell patch-clamp configuration. Microglial cells were targeted via their intrinsic GFP signal across the hippocampal CA1-CA3 stratum lacunosum-moleculare and stratum radiatum regions.

G. Resting membrane potential (left) and input resistance (right) of individual microglial cells at different timepoints of the recovery process. N=10 animal, p.n.: ~90 days; N=158 cells measured in total; independent t-test, ns: not significant, *: $p<0.05$, **: $p<0.01$, ***: $p<0.001$.

Immediate release of ATP and sustained ATP fluctuations contribute to microglial phenotype changes in a P2Y12R dependent manner

Since injury-induced ATP markedly affects microglial phenotypes and recruitment via P2Y12R (Davalos et al., 2005; Haynes et al., 2006), we set out to examine extracellular ATP levels in acute brain slices by generating a novel mouse strain expressing a sensitive, genetically-encoded fluorescent ATP sensor ($GRAB_{ATP}$) in VGlut1 positive neurons (Z. Wu et al., 2022). In order to capture time-dependent extracellular ATP dynamics, we recorded 10 min long videos via two-photon imaging, as well as confocal Z-stacks from both regions of cortex and hippocampus in each hour after the slice preparation (Fig 5A). We observed high fluorescent signals, representing extracellular ATP levels both in the hippocampal CA3 region and in cortical layers shortly after cutting (Fig 5B), which was most intense near the slice surface, as revealed by Z stack acquisitions. The mean ATP signal rapidly declined in the first 10 minutes of imaging (Fig 5B-C; Suppl. Fig 2A), corresponding to the 10-20 min interval upon slice preparation (see: Fig.5.A and Methods). Then on, ATP levels showed a slow, gradual decrease (Fig 5D, F; Suppl. Fig 2B; Supplementary Video 5) with ATP gradient maintained through the 0-100 µm depth of the tissue for at least 5 hours (Suppl Fig 2C). While ATP release from brain slices generally decreased over time, we also observed intense, focal ATP flashes throughout the 5 hours period after slice preparation (Supplementary Video 5; Fig 5E). ATP flash incidence in acute slices was 12.3±2.2 (hippocampus) and 25.4±5.2 (cortex) during the 10 min imaging periods, resembling systemic inflammation-induced flashing activity *in vivo* (Z. Wu et al., 2022) (Fig.5.H, Suppl. Fig 3A). While we detected more frequent and intense ATP flashes in cortical regions of acute slices than in the hippocampus (Fig 5 G-H), all other characteristics (ATP flash area, duration, rise time, decay time) were quite uniform (Suppl. Fig 3B), in agreement with earlier observations (Z. Wu et al., 2022). It should be noted, however, that the observed intensity differences across different depth of slices may also be affected by the heterogenous sensor expression.

In order to directly test whether purinergic signaling would play a role in the observed migration and morphological changes of microglia, we prepared samples from wild-type, P2Y12R-KO and PSB0739 (PSB, a selective P2Y12R-inhibitor) treated wild-type mice, where PSB (10 µM) was present

327 both in the cutting and incubating solutions during slice preparation. Time series of slices were prepared
328 and fixed as previously. We found that the time course of the changes, including microglial sphericity
329 and number of ending nodes, as well as dislocation and process redistribution of microglia were
330 disrupted significantly by the absence or inhibition of P2Y12Rs (Fig 5I and J), (Fig 5J), suggesting that
331 microglial phenotypic changes during slice incubation are influenced by extracellular ATP (ADP) via
332 P2Y12R.

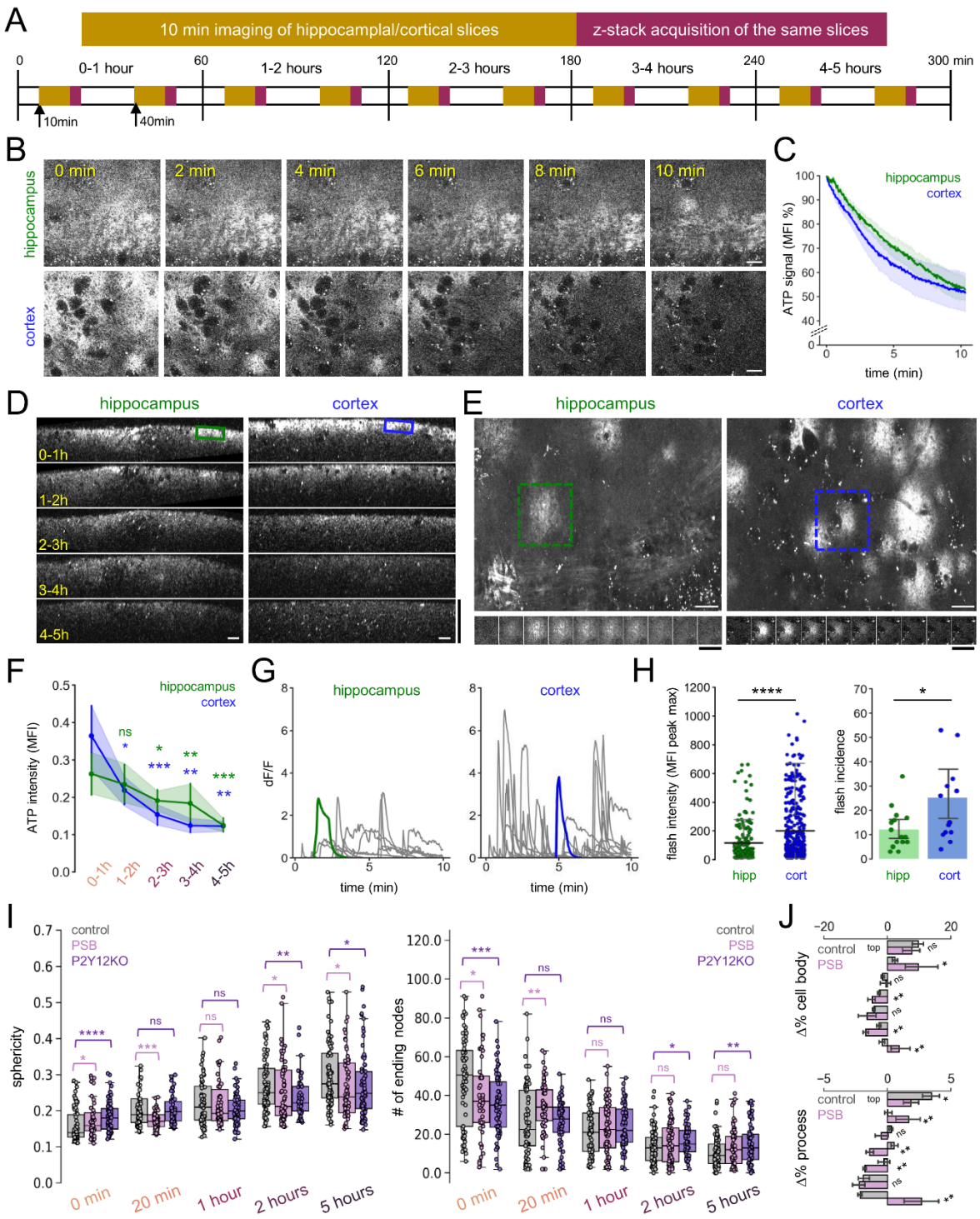

Figure 5. Immediate release of ATP and sustained ATP fluctuations contribute to microglial phenotype changes in a P2Y12R dependent manner

A. Outline of the two-photon imaging experiment performed on acute brain slices. Slices were prepared from mice expressing the ATP sensor (GRAB$_{ATP}$ on the cell surface of VGlut1-positive neurons to measure changes in extracellular ATP levels. 10 min-long imaging sessions were followed by Z-stack acquisition after slice cutting, for up to 5 hours. Altogether, 3*5 hippocampal (CA3) and 3*5 cortical (layer 2-3) data sets were collected from n=3 mice 1 hour apart.

B. Representative images of the video sets taken at the earliest manageable timepoint after slice cutting. Scale bar: 20 µm.

C. MFI data indicating a continuous and significant decrease of the extracellular ATP signal in regions with no flashing ATP activity (Two-way repeated measures ANOVA, $F(1.221, 23.20)=71.63$, ****$P<0.0001$). A gradual, slow decrease of ATP signal was observed in subsequent timepoints (see Suppl. Fig 2A).

D. Representative side-views of Z stacks show marked ATP production next to the slice surface (0-25µm) showing a time-dependent decrease of the signal towards the 5 hours' timepoint. Horizontal scale bar: 20 µm, vertical scale bar: 125 µm.

E. Maximum intensity projection images of representative videos show the occurrence of ATP flashes. Below the images the timeline of two individual ATP flashes are shown (10 sec/image). White scale bar: 20 µm, black scale bar: 10 sec.

Quantification of the MFI measurements shown in D, as ATP levels are following a significant, time-dependent decrease towards the 5 hours' timepoint. Two-way repeated measures ANOVA with Tukey's multiple comparison test; data are compared to 0-1h values for either cortex or hippocampus: *:$p<0.05$, **:$p<0.01$, ***:$p<0.001$

F. Corresponding dF/F graphs depict flashing activity at the same fields as shown in E.

G. The intensity of the ATP flashes is significantly higher in cortical slices (n=360) than in hippocampal ones (n=181). Mann-Whitney test, ****$p<0.0001$. The incidence of flashes is higher in cortical slices. The number of ATP flash/10min imaging/slice are shown. Unpaired t-test, $P=0.0258$.

H. Quantification of extracted morphological features showing significant differences between control and P2Y12KO or PSB treated acute slices regarding the sphericity (left) and the number of ending nodes/cell (right). N=2 animal/lab, p.n.: ~65 days; Mann-Whitney, ns: not significant, *: $p<0.05$, **: $p<0.01$, ***: $p<0.001$, ****: $p<0.0001$.

I. Bar plots showing the differences between control and PSB treated acute slices. Changes of microglial cell body percentages (top) and area covered by processes (bottom) are calculated between 0 min and the 5 hours across the top and bottom layers of acute slice preparations. N=2 animal/lab, median ± SEM, Mann-Whitney, ns: not significant, *: $p<0.05$, **: $p<0.01$.

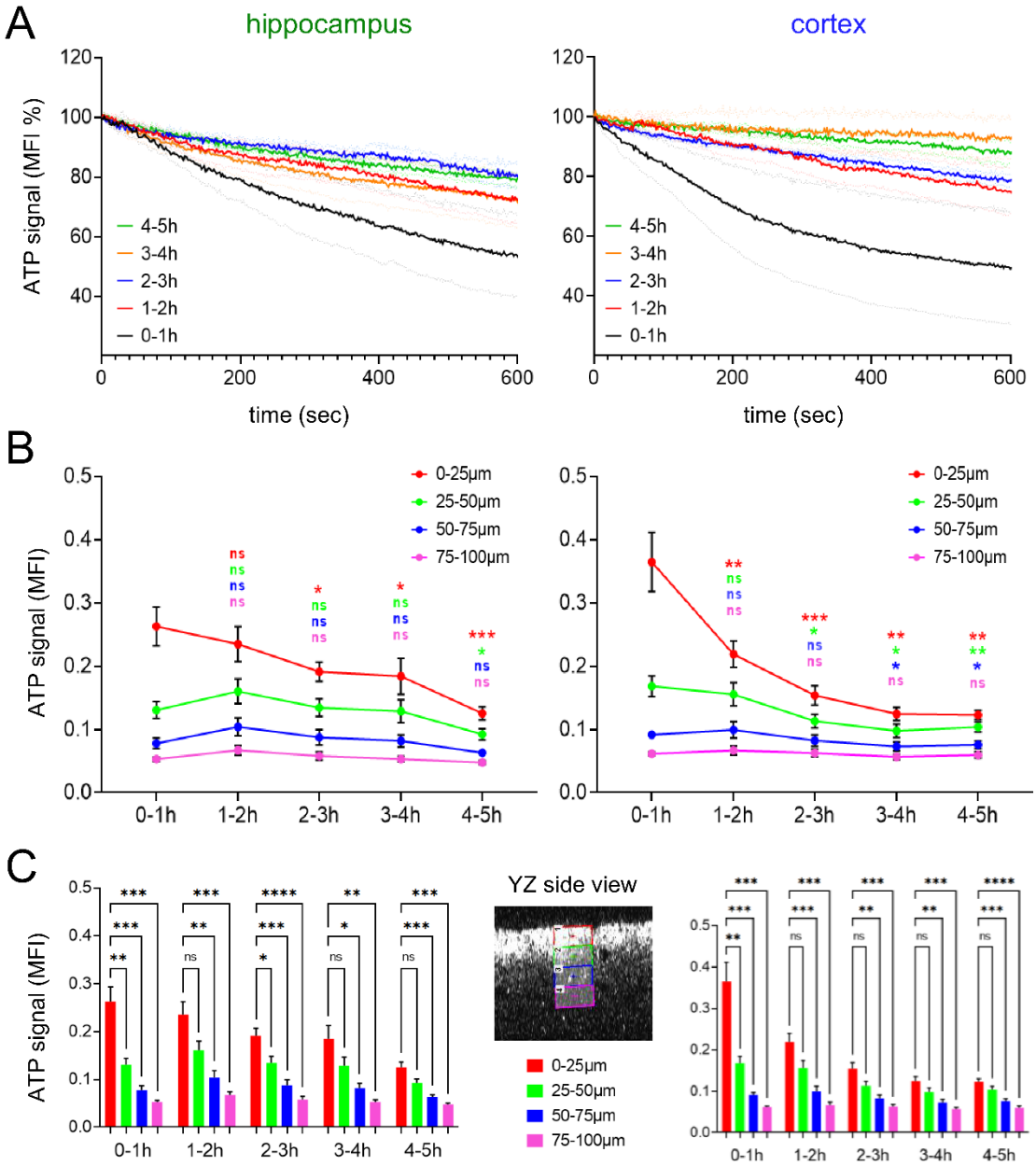

Supplementary Figure 2. Characteristics of extracellular ATP signal changes in acute brain slices

A. MFI data collected from hippocampal or cortical slices imaged 1-2h (red), 2-3h (blue), 3-4h (orange) or 4-5 (green) hours after slice preparation show significantly slower ATP reduction, than those from the earliest timepoints (0-1h, black). Note, that data were collected from regions of interests where no apparent flashing ATP activity was observed. Two-way ANOVA, ****P<0.0001 for all (red, blue, orange, green) compared to 0-1h (black).

B. MFI data obtained from Z stacks. ATP signal intensity and subsequent reduction over time is most apparent next to the slice surface (0-25, 25-50um) compared to deeper layers (75-100um). Two-way repeated measures ANOVA, Dunnett's multiple comparison test.

C. Gradient in ATP signal intensity from the slice surface to the ~100 µm depth of the slice is maintained for at least 5 hours after slice preparation. Two-way repeated measures ANOVA, Dunnett's multiple comparison test.

A

	ATP flash incidence [number of events/10min]	peak intensity [MFI]	peak area [μm²]	peak duration [sec]	rise time [sec]	decay time [sec]
hippocampus	12.3 ± 2.2 n=15	116.1± 10.2 n=181	229.1± 16.5 n=151	88.9± 5.9 n=156	15.02 ± 1.4 n=178	75.8 ± 5.3 n=155
cortex	25.4 ± 5.2 n=15	200.8 ± 11.6 n=360	243.1 ± 13.9 n=309	81.9± 3.8 n=318	12.2 ± 0.7 n=369	70.6 ± 3.4 n=318
	unpaired t-test *p=0.0258	Mann-Whitney test ****p<0.0001	Mann-Whitney test p=0.3912	Mann-Whitney test p=0.3803	Mann-Whitney test p=0.2474	Mann-Whitney test p=0.4207

B

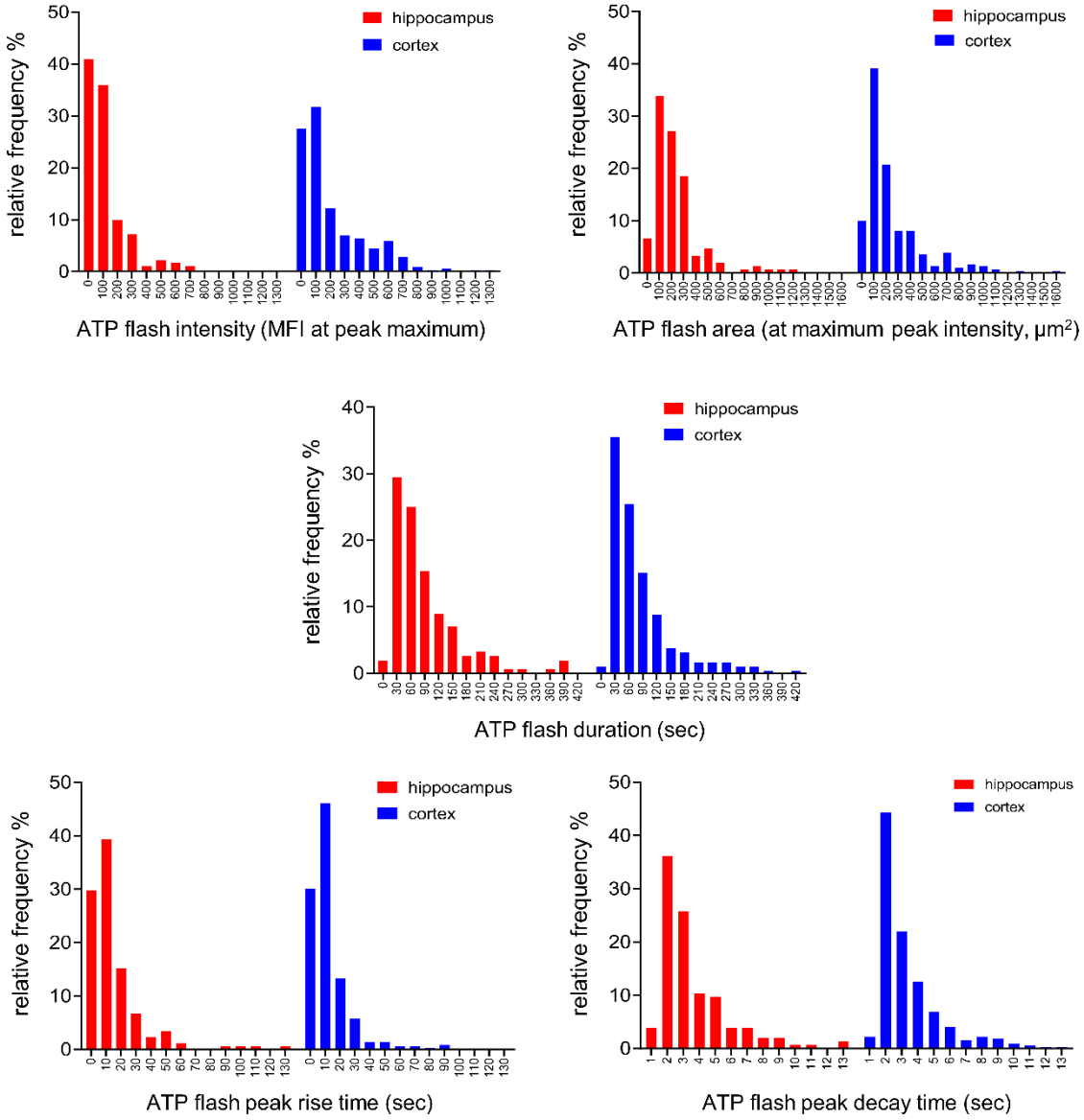

379 **Supplementary Figure 3. Properties of ATP flash events in acute slices**

380 A. Statistics of ATP flash properties.

381 B. Histograms show data distribution of flash intensity, area, duration, rise time and decay time.

Rapid changes of microglia-neuron interactions and microglia-dependent synaptic sprouting characterize acute slices

Next, we investigated whether changes in microglial phenotype parallel altered microglia-neuron interactions in acute slice preparations. To this end, we looked at microglial contacts with synaptic elements and neuronal cell bodies (Cserép et al., 2020), in order to examine how the number of these contacts might change during the incubation process. The native GFP-signal of microglia was enhanced by anti-GFP labelling, while neuronal cell bodies were identified via Kv2.1 labelling. Synaptic elements were further identified via VGLUT1-Homer1 and VGAT-Gephyrin co-localization (Fig 6A,C). We found that the total percentage of neuronal soma contacted by microglial processes gradually decreased throughout the incubation process and dropped by ~23% (Mann-Whitney, $p<0.01$) after 5 hours of incubation (Fig 6B, left). We also investigated the percentage of somatic area covered by microglial processes over time, which has doubled at 0 minutes (fixed immediately after cutting) compared to the perfused controls (from 4% to 8%, $p<0.05$). This observation indicates extremely rapid microglia actions taking place during the ~1-3 minutes between brain extraction and slice fixation. The massive initial increase was followed by a gradual decrease dropping back again to control values (purple indication; $p<0.05$) after 5 hours of incubation (Fig 6B, right). In line with this, microglia-synapse contact prevalence showed similar alterations after slice preparation in the case of glutamatergic synapses (Fig 6D, left), where average percentage of contacts increased by 46% between the perfused and 0-minute conditions ($p<0.05$) and gradually dropped back to control values. In the case of GABAergic synapses (Fig 6D, right), we did not observe significant increase immediately after slice preparation, however we measured a prominent decrease in contacts during the incubation process, with a 36% drop after 2 hours of incubation ($p<0.01$). Based on these observations, we concluded that microglia-neuron interaction sites underwent rapid and progressive changes, as somatic coverage and contact prevalence on glutamatergic synapses significantly increased immediately after slice preparation, followed by a gradual decrease over time.

Given the observed changes in microglial contact prevalence on synapses, we next examined how the density of synaptic elements changed during the incubation process. We used the quantitative post-embedding labelling method to precisely determine both glutamatergic and GABAergic synaptic

410 density changes (Fig 6E) in acute slices. We found significant increases in both glutamatergic (20%
411 increase compared to 0 min, $p<0.01$) and GABAergic (9% increase compared to 0 min, $p<0.05$) synaptic
412 density after 1 hour of incubation (Fig 6F), similarly to previous reports (Bourne et al., 2007; Kirov et
413 al., 1999; Trivino-Paredes et al., 2019). Interestingly, measuring synapse density at multiple timepoints
414 during the incubation process revealed robust time-dependent changes concerning the proportions of
415 excitatory and inhibitory synapses. While we observed similar, gradual increase in glutamatergic and
416 GABAergic synaptic density towards the 1- and 2-hour timepoints, there was a 1-hour lag in the case
417 of GABAergic synapses (Fig 6F, left vs. right), which peaked after 2 hours of incubation (20% increase
418 compared to 0 min, $p<0.001$). Coincidentally, we observed a significant drop in glutamatergic synaptic
419 density which occurred between 1- and 2 hours of incubation (Fig 6F left, purple statistical indication;
420 9% drop, $p<0.05$). We observed the highest density of glutamatergic synapses after 5 hours (28%
421 increase compared to 0 min, $p<0.01$), whereas at this timepoint there was a tendency of decrease in
422 GABAergic synaptic density (Fig 6F right; pink statistical indication; 10% drop, n.s., $p=0.051$). Based
423 on these observations, we concluded that the neuronal network is likely to be reorganized by the slow
424 and gradual build-up of excitatory synapse numbers, which is followed by the inhibitory synapses in
425 the same manner. The inhibitory sprouting seemed to reach its maximum after 2 hours of incubation,
426 while excitatory synapse numbers further increased towards the 5-hour timepoint.

427 Increasing evidence suggests that microglial cells are essential for the formation, pruning and
428 maintenance of synapses both in the developing and in the adult CNS (Ikegami et al., 2019). We wanted
429 to examine whether microglia can also actively contribute to the observed time-dependent structural
430 and functional changes in synaptic density detected in acute slice preparations. To this end, we measured
431 changes of synaptic densities in acute slice preparations in the absence of microglia (induced by
432 elimination of microglia with PLX5622 for three weeks *in vivo* prior to slice preparation, Fig 6G-H).
433 Depletion of microglia with PLX3373 or PLX5622 *in vivo* has previously been shown to induce no
434 substantial changes in neuronal cell numbers and morphology, nor did it cause any deficits in cognition
435 and behaviour, although dendritic spine numbers showed a slight increase (Elmore et al., 2014; Han et
436 al., 2017; Strackeljan et al., 2021). To measure and compare synaptic density changes between control
437 (CTRL) and depleted (DEPL) condition, we used the previously described post-embedding labelling

438 method (Fig 6I). We found that time-dependent synaptic density changes after slice preparation were
439 markedly influenced by microglial actions (Fig 6J). To our surprise, the absence of microglia abolished
440 the gradual increase of glutamatergic synaptic density observed under control conditions and resulted
441 in significantly lower synapse densities from 20 minutes after slice preparation and onward, reaching
442 27% lower synaptic density values in DEPL compared to CTRL after 5 hours, ($p<0.001$, Fig 6D, left).
443 Even more prominent differences were observed regarding GABAergic synaptic densities (Fig 6J,
444 right). The absence of microglia led to a marked initial increase of GABAergic synaptic density, peaking
445 at 1 hour, followed by significant drop at 2 hours. This course fundamentally differs from that observed
446 under control conditions, which peaks at 2 hours (19% higher in CTRL, $p<0.001$, Fig 6J, right). These
447 results clearly indicate that microglia differentially control excitatory and inhibitory synaptic sprouting
448 in acute slice preparations, initiating glutamatergic, while repressing GABAergic synapse formation,
449 during the early stages (<1hour) following acute slicing.

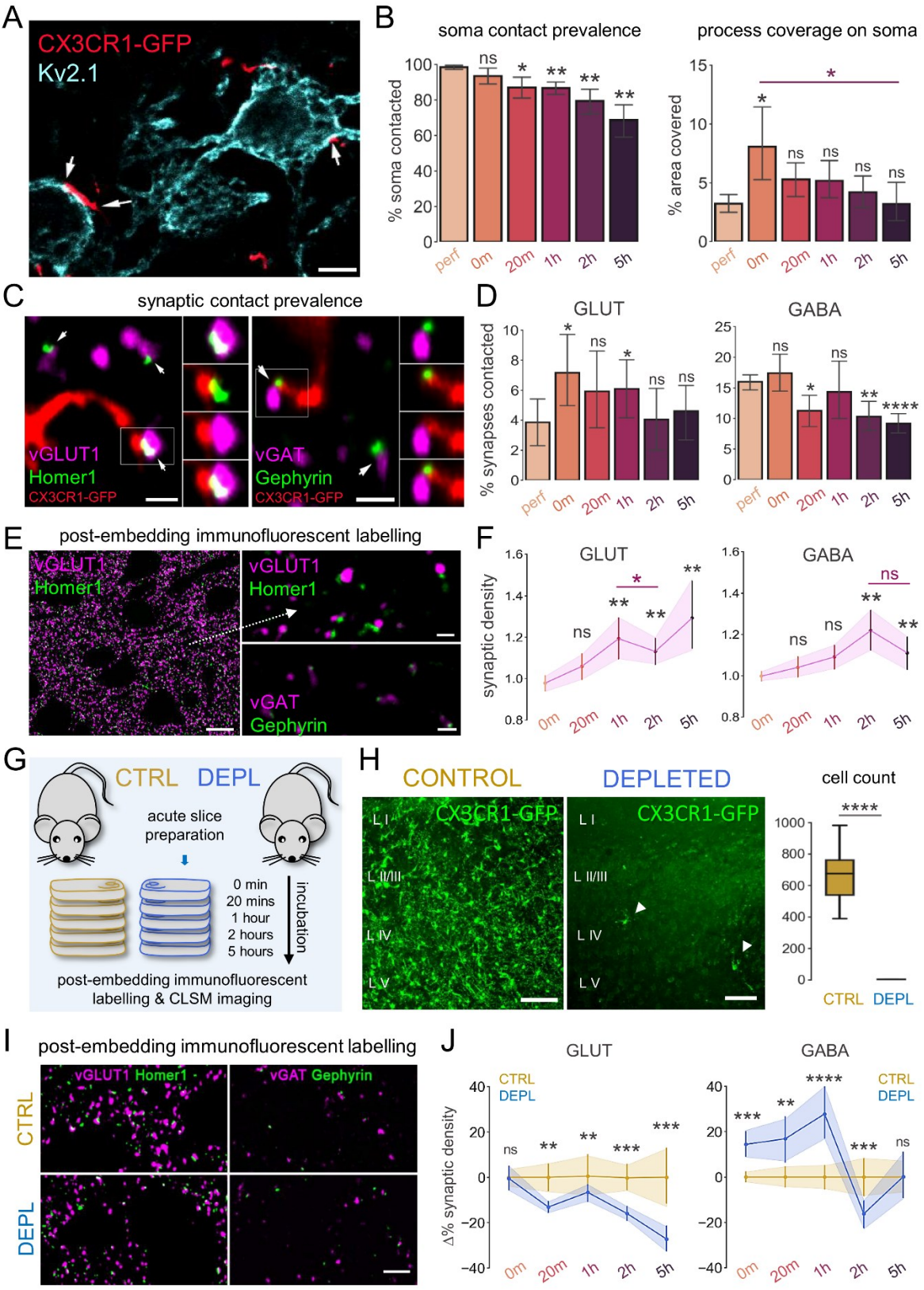

Figure 6. Microglial phenotype changes are accompanied by rapid alterations of microglia-neuron interactions and microglia-dependent synaptic sprouting

A. Representative section of a maximum intensity projection image created from confocal z-stacks used to quantify microglial contact prevalence and process coverage on neuronal soma. White arrows point to areas

454 (overlap of microglia and Kv2.1 labelling) where microglial processes are likely to form contacts on neuronal
455 soma (Scale bar: 5 µm).
456 B. Quantification of contact prevalence (left) and coverage (right) of neuronal soma by microglial processes
457 (left). N=3 animal, p.n.: ~90 days; Mann-Whitney, ns: not significant, *: p<0.05, **: p<0.01, ***: p<0.001.
458 Black statistical indication: perfused values vs. 0 min – 5 hours. Purple statistical indication: 0 min vs. 5
459 hours.
460 C. Single image planes from confocal z-stacks used to quantify contact prevalence of microglial processes onto
461 glutamatergic (left) or GABAergic (right) synapses. (Inserts show image channel pairs from the boxed area,
462 from top to bottom: pre- and postsynaptic marker, microglia and postsynaptic marker, microglia, and
463 presynaptic marker, merged.) Arrows show identified individual synapses contacted by microglial processes
464 (bars: 1 µm).
465 D. Quantification of microglial contact prevalence onto glutamatergic (left) or GABAergic (right) synapses. N=3
466 animal, p.n.: ~90 days; Mann-Whitney, ns: not significant, *: p<0.05, **: p<0.01, ****: p<0.0001.
467 E. Representative sections of maximum intensity projection images created from confocal z-stacks used to
468 quantify glutamatergic and GABAergic synaptic densities. Images were created using the post-embedding
469 labelling technique. A large area of glutamatergic synaptic labelling is shown (left, bar: 5 µm) and zoomed-
470 in insets of glutamatergic (right, top; bar: 1 µm) and GABAergic synaptic labelling (right, bottom; bar: 1 µm).
471 F. Quantification of synaptic density changes during the incubation process regarding glutamatergic (left) and
472 GABAergic (right) synapses. N=6 animal, p.n.: ~65 days; Mann-Whitney, ns: not significant, *: p<0.05, **:
473 p<0.01, ***: p<0.001.
474 G. Schematic representation of experiment. CX3CR1$^{+/GFP}$ littermates were used to create a control (CTRL; N=3,
475 p.n.: ~65; brown) and microglia depleted (DEPL; N=3, p.n.: ~65; blue) subgroup of animals. Slice preparations
476 were obtained from both groups and immersion-fixed at different timepoints during recovery.
477 H. Maximum intensity projection images showing microglial cells in acute slice preparations obtained from
478 animals that either belong to control (left) or depleted (middle) group (bars: 100 µm). Quantification
479 comparing the total number of microglial cells counted in control (CTRL, brown) or depleted (DEPL, blue)
480 acute slices (right). N=6-6 animal, p.n.: ~65 days; Mann-Whitney, **: p<0.01.
481 I. Representative sections of maximum intensity projection images created from confocal z-stacks used to
482 quantify and compare densities of glutamatergic (left) or GABAergic (right) synapses in control (top row) or
483 microglia depleted (bottom row) acute slices (bar: 5 µm).
484 J. Comparison of synaptic density changes during the incubation process regarding glutamatergic (left) and
485 GABAergic (right) synapses between control and microglia depleted animals. The percentage of changes
486 compared to the average values measured in control mice (brown, data also shown in panel F) are shown
487 with changes calculated for microglia depleted (blue) acute slices. N=6 animal, p.n.: 65 days; Mann-Whitney,
488 ns: not significant, **: p<0.01, ***: p<0.001, ****: p<0.0001.

The absence of microglia or microglial P2Y12 receptors dysregulates neuronal network activity in acute slice preparations

It is well known that slices need a recovery period after cutting, to enable reliable and stable electrophysiological measurements. In line with this, we observed significant increase in SWR parameters after 2 hours in control slices (Supp. Fig 4), which paralleled marked, time-dependent changes in GABAergic and glutamatergic synapse densities.

Because the absence of microglia resulted in markedly lower glutamatergic and GABAergic synaptic densities after 2 hours of incubation (Fig 6J), we set out to examine whether synchronous events are also positively affected by the presence of microglia and compared features of spontaneously occurring SWR activity measured from control (CTRL), or microglia depleted (DEPL) acute slice preparations (Fig 7A-B). Simultaneous recordings from both conditions allowed precise quantification and comparison of the differences concerning the occurrence of SWR activity between the two conditions. We observed that 18 out of 36 slices (50%) presented detectable SWR activity in CTRL, whereas only 4 out of 36 slices (11%) from DEPL (Fig 7C). This striking difference confirms that microglial actions are necessary for the emergence of physiological-like network activity in *ex vivo* slices. Furthermore, our results showed significant differences between spontaneously occurring SWR activity recorded from CTRL or DEPL acute slice preparations, as we observed ~3.5-fold decrease in SWR amplitude, ~1.9-fold decrease in SWR rate and ~2.1-fold decrease in ripple amplitude registered from DEPL when compared to CTRL slices (Fig 7D). These results indicate that microglia can effectively support the neuronal network in slice preparations during the incubation process, and can positively influence the occurrence, amplitude, and frequency of spontaneously occurring SWR activity.

To examine whether P2Y12 mediated actions are contributing to the observed effects, we repeated the same experiment by comparing slices from control and P2Y12 KO mice (Fig 7E-F). Similarly to microglia depleted mice, SWR occurrence was lower in the absence of P2Y12Rs (Fig 7G, 33%, 10 slices from 30 in total) when compared to control slices (46.6%, 14 slices out of 30). In this case, we also observed significant differences in SWR parameters, as SWR amplitude in average showed a ~1.7-fold decrease (Fig 7H, left), while SWR ripple amplitude showed ~1.3-fold decrease in

517 P2Y12 KO animals (Fig 7H, right). SWR rate also decreased ~1.3-fold compared to control slices,
518 however due to a higher variance, this difference was not significant (Fig 7H, middle). Taken together,
519 these results suggest that the positive influence of microglia on SWR activity observed in acute slice
520 preparations is in part mediated by microglial P2Y12R action.

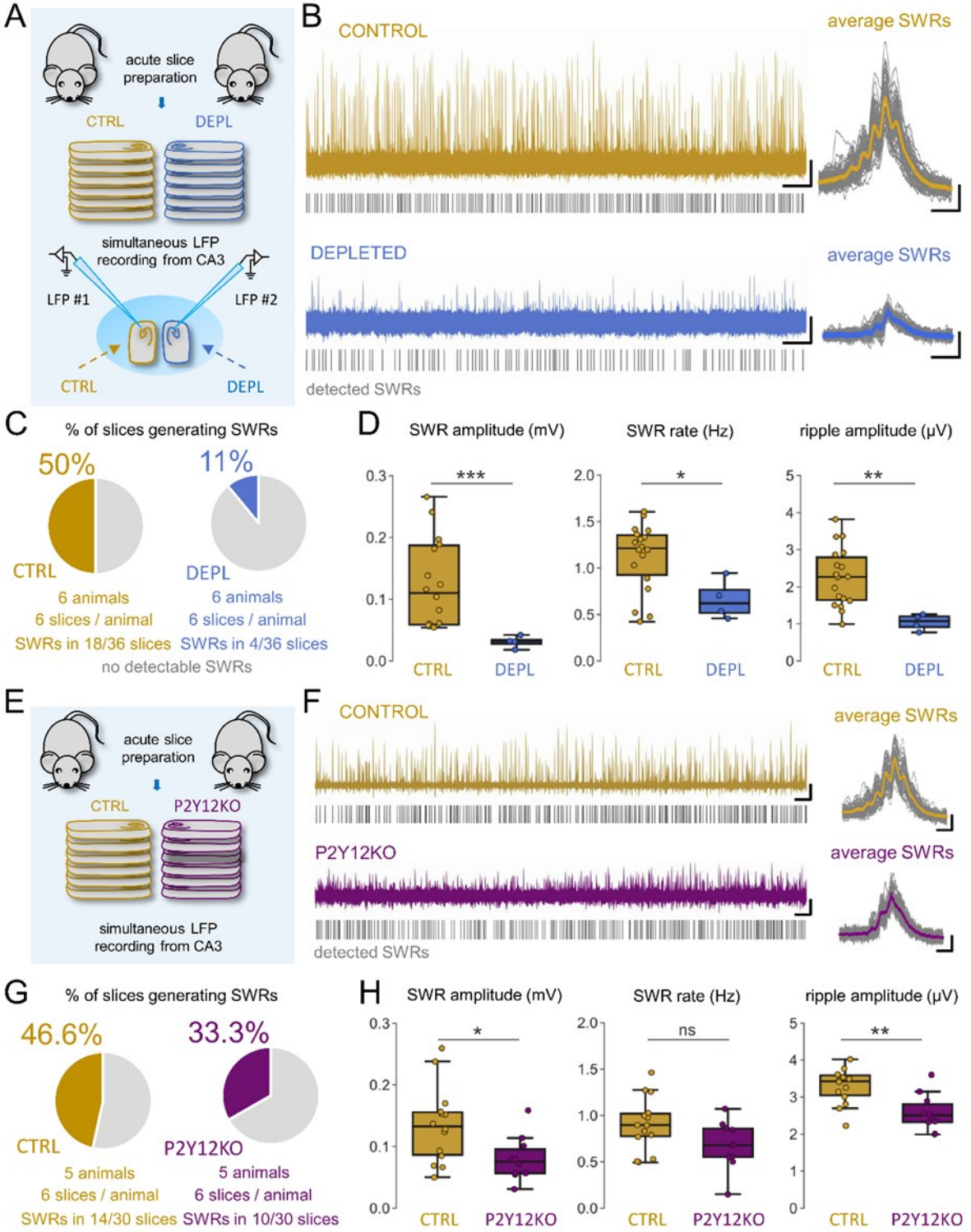

Fig 7. The absence of microglia or microglial P2Y12 receptors dysregulates neuronal network activity in acute slice preparations

A. Schematic representation of experiment. CX3CR1$^{+/GFP}$ littermates were subjected to 3 weeks of either control or PLX3397 containing diet to create a control (CTRL; N=6, p.n.: ~65; brown) and microglia depleted (DEPL; N=6, p.n.: ~65; blue) subgroup of animals. Acute hippocampal slice preparations were obtained from both groups and placed into an interface-type incubation chamber for at least 1 hour of recovery. Subsequently, slices were transferred together in a pairwise manner into a recording chamber, to simultaneously measure sharp wave-ripple (SWR) activity via local field potential recordings (LFP) registered from the CA3 pyramidal layer of the hippocampus.

B. Representative LFP recordings (left; bar: 30 s, 50 µV) and averages of spontaneous SWR events (right; #50 in total, bar: 100 ms, 25 µV) registered from control (top row, green) and microglia depleted (bottom row, blue) slices. Grey lines represent detected SWR events.

C. Pie-charts representing SWR activity occurrence in slices measured from control group (green, 18/ 36 slices) versus microglia depleted (blue, 4/36 slices).

D. Quantification of SWR amplitude (left), rate (middle) and Ripple amplitude (right) comparing events measured from control (CTRL, green) or depleted slices (DEPL, blue). Quantification showed a median value of SWR amplitude (in mV, 1st quartile, 3rd quartile) 0.109 (0.058, 0.191) in the case of CTRL and 0.032 (0.021, 0.04) in the case of DEPL conditions (Mann-Whitney test, $p<0.001$). Concerning SWR rate, we measured (in Hz) 1.21 (0.86, 1.37) in CTRL condition, and 0.62 (0.47, 0.88) in case of DEPL condition ($p<0.05$). We measured the Ripple amplitude to be (in µV, 1st quartile, 3rd quartile) 2.27 (1.59, 2.86) in the case of CTRL and 1.07 (0.82, 1.23) in the case of DEPL conditions ($p<0.01$). N=6 animal/group, p.n.: ~65 days; Mann-Whitney test, ns: not significant, *: $p<0.05$, **: $p<0.01$, ***: $p<0.001$.

E. Schematic representation of experiment. Control (CTRL; N=5, p.n.: ~65; brown) and P2Y12 KO mice (DEPL; N=6, p.n.: ~65; purple) were examined during the experiments, similarly as described in A. Acute hippocampal slice preparations were obtained from both groups and placed into an interface-type incubation chamber for at least 1 hour of recovery. Subsequently, slices were transferred together in a pairwise manner into a recording chamber, to simultaneously measure sharp wave-ripple (SWR) activity via local field potential recordings (LFP) registered from the CA3 pyramidal layer of the hippocampus.

F. Representative LFP recordings (left; bar: 30 s, 50 µV) and averages of spontaneous SWR events (right; #50 in total, bar: 100 ms, 25 µV) registered from control (top row, brown) and P2Y12 KO (bottom row, purple) slices. Grey lines represent detected SWR events.

G. Pie-charts representing SWR activity occurrence in slices measured from control group (brown, 14/ 30 slices) versus P2Y12 KO (purple, 10/30 slices).

H. Quantification of SWR amplitude (left), rate (middle) and Ripple amplitude (right) comparing events measured from control or P2Y12 KO slices. Quantification showed a median value of SWR amplitude (in mV, 1st quartile, 3rd quartile) 0.133 (0.087, 0.155) in the case of CTRL and 0.075 (0.057, 0.096) in the case of P2Y12 KO (Mann-Whitney test, $p<0.05$). Concerning SWR rate, we measured (in Hz) 0.89 (0.77, 1.02) in CTRL, and 0.68 (0.55, 0.85) in case of KO ($p=0.14$). We measured the ripple amplitude to be (in µV) 3.42 (3.04, 3.58) in the case of CTRL and 2.51 (2.32, 2.81) in the case of KO ($p<0.01$). N=5 animal/group, p.n.: ~65 days; Mann-Whitney test, ns: not significant, *: $p<0.05$, **: $p<0.01$.

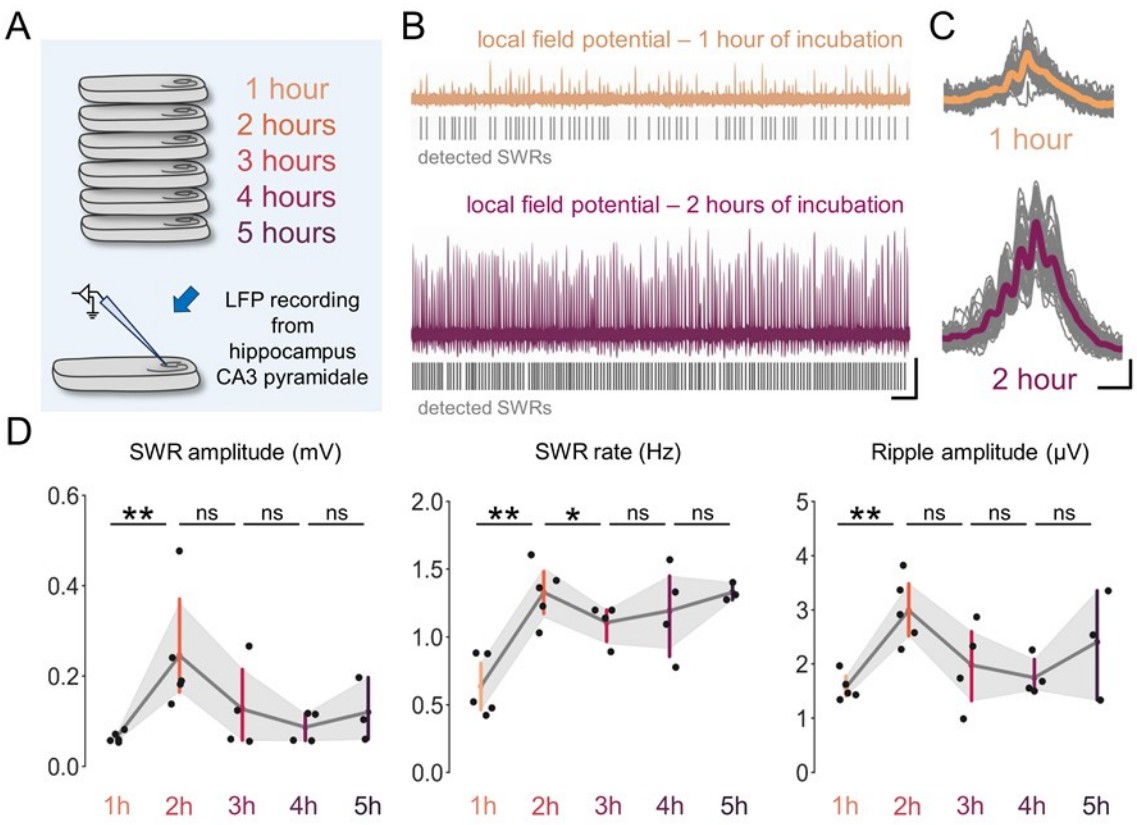

Supplementary Figure 4. Temporal course of the emergence of Sharp Wave-Ripple activity after acute slice preparation

A. Schematic representation of the experiment. CX3CR1$^{+/GFP}$ littermates (N=8; p.n.: ~65 days) were used to create acute hippocampal slice preparations and placed into an interface-type incubation chamber for at least 1 hour of recovery time. Subsequently, slices were transferred at specific timepoints (hourly after 1-5 hours) into a recording chamber to measure sharp-wave ripple (SWR) activity via local field potential recordings (LFP) registered from the CA3 pyramidal layer of the hippocampus.

B. Representative LFP recordings measured after 1 (yellow) or 2 hours (purple) of incubation. Grey lines represent detected SWR events (bars 10 s, 50 µV).

C. Representative averaged traces of detected SWRs (#50 in total) measured after 1 hour (yellow: average, grey: individual events) or 2 hours (purple: average, grey: individual events) of incubation (bars 100 ms, 25 µV).

D. Quantification of SWR amplitude (left), rate (right) and Ripple amplitude (right) comparing events measured after different time spent in the incubation chamber before recording. N=8 animal, p.n.: 65 days; Kruskal-Wallis test, ns: not significant, *: $p<0.05$, **: $p<0.01$.

Discussion

In this study, we provide a comprehensive assessment of microglial function in acute slice preparations in an experimentally relevant timeframe, using sample sets from multiple expert laboratories. We show that while microglia are undergoing marked time-dependent phenotype changes, they are instrumental to maintain *ex vivo* spontaneous activity of the neuronal network in a P2Y12R-dependent manner. We believe that these fundamental mechanisms of microglia-neuron interactions should be considered for studies on microglial and neuronal functions *ex vivo*, while also have important implications for the acute slice methodology and could facilitate improvements in modelling.

We first studied how the slice preparation procedure affected microglial cells in acute slices. While locomotor and process polarization behaviour of microglia in slice preparations have been previously suggested (Petersen & Dailey, 2004; Stence et al., 2001), population level changes in the distribution of cell bodies and processes along the full depth of slices have not been investigated in a time-dependent manner before. Because microglia are extremely sensitive to tissue disturbance, the acute slice preparation technique can ultimately be considered as a traumatic event assumed to influence microglial function, as observed in acute slices prepared via different methodologies (Kettenmann et al., 2011; Matyash et al., 2017; Petersen & Dailey, 2004; Stence et al., 2001). Of note, in comparison with other studies, microglia after 1 hour of incubation showed extremely similar morphological characteristics to cells measured at peri-infarct cortical areas in experimental stroke models (Heindl et al., 2018; Morrison & Filosa, 2013; Sadler et al., 2020; Singh et al., 2018). Moreover, the difference in the number of microglial process endings observed in a study comparing control and Alzheimer's disease patients (Davies et al., 2017), closely resembles the changes that we observed in acute slices (~50% drop) as early as after 20 minutes of incubation.

It has been previously suggested that gradually decreasing levels of oxygenation along the depth of the slice, as well as higher neuronal activity at the top surface could mediate injury-related signals (Huchzermeyer et al., 2013; Ivanov & Zilberter, 2011; Mulkey et al., 2001). Importantly, microglial phenotype changes were found to represent a generic response to slice preparation, as different slice preparation techniques carried out in independent laboratories consistently resulted in a

gradually increasing density of reactive microglia both at slice surfaces and in deeper layers. While our observations reinforce general guidelines in electrophysiological investigations to avoid measurements taking place at the top 30-50 µm of slice preparations (Avignone et al., 2019), they provide novel mechanisms explaining the marked regional- and time-dependent heterogeneities observed in acute slices. Microglial recruitment to the site of injury and morphological transformation are known to be driven by extracellular ATP (which quickly hydrolyses to ADP) and P2Y12R actions (Davalos et al., 2005; Haynes et al., 2006; Nasu-Tada et al., 2005), which we assumed to take place upon slice preparation. To this end, we used a newly developed mouse line, where glutamatergic neurons express fluorescent ATP-sensor in the plasma membrane, enabling the visualisation of extracellular ATP-levels throughout the neuropil. While our results showing massive ATP-levels close to the cut slice surfaces were somewhat expected, we also reveal that the ATP-gradients are likely to drive microglial dislocation and morphological changes via P2Y12R throughout the slices, including deeper tissue locations. Initial ATP release effects could be further augmented by sustained ATP-flashes deep in the slices even hours after slice cutting. Such flashing ATP activity was also observed after acute brain injury *in vivo* (Chen et al., 2022). Important questions for future research will be how these local changes in extracellular ATP levels could influence microglial and neuronal physiology in *ex vivo* slice preparations.

P2Y12 receptors (P2Y12R) not only represent a core marker for microglia in the healthy brain (Bosco et al., 2018; Hickman et al., 2013; Peng et al., 2019), but downregulation of P2Y12R is associated with reactive phenotypes and microglial dysfunction both *in vivo* and *ex vivo* (Cserép et al., 2020; Gu et al., 2016; Haynes et al., 2006; Lin et al., 2021; Zrzavy et al., 2017). We show with a fully quantitative post-embedding method (Holderith et al., 2020) that rapid downregulation of P2Y12R occurs most extensively at the processes of microglia already after 1 hour of incubation proportionally with marked morphological changes. Resting membrane potential of microglia has also been shown to correlate with morphology, as modified activity of tonically active K+ channels responsible for maintaining resting membrane potential (knocking out THIK-1 or locally increasing extracellular [K+]) can decrease ramification (Madry, Arancibia-Cárcamo, et al., 2018; Madry, Kyrargyri, et al., 2018). It has been proposed that transitioning into a more reactive phenotype could partly reflect decreased

628 expression of THIK-1 (Madry, Kyrargyri, et al., 2018), as activation via LPS treatment resulted in a
629 significantly downregulated expression of THIK-1 mRNA (Holtman et al., 2015). Importantly, our
630 results indicate that gradual depolarization, rapid P2Y12R downregulation and transitioning into a
631 reactive morphology are co-occurring events in acute slice preparations solely at "baseline" conditions,
632 which have important implications for models using acute slice preparations.

633 Changes in microglial distribution, morphology, P2Y12R-expression and local ATP fluxes are
634 expected to markedly influence cell-cell interactions, given that P2Y12R signalling is required for
635 normal microglial interactions with neuronal somata and synapses under different conditions (Cserép
636 et al., 2020; Lin et al., 2021; Miyamoto et al., 2016; Sipe et al., 2016). We showed that while the
637 prevalence of contacts on neuronal soma (somatic junctions) slowly and gradually decreases, the
638 percentage of somatic area covered by microglial processes undergoes a more than two-fold increase
639 immediately after slice preparation similarly to that observed *in vivo* after acute ischemia (Cserép et al.,
640 2020). These changes paralleled increased numbers of contacts on glutamatergic synapses, while
641 contacts on GABAergic synapses were gradually decreasing. Studies have previously demonstrated that
642 acute slice preparation induces synaptic sprouting (Bourne et al., 2007; Kirov et al., 1999; Trivino-
643 Paredes et al., 2019), but the mechanisms of these changes have not been revealed. Microglia are well-
644 known regulators of synaptic density *in vivo* (Akiyoshi et al., 2018; Miyamoto et al., 2013, 2016;
645 Schafer et al., 2013; Wake et al., 2009; Y. Wu et al., 2015). Of note, we found that the absence of
646 microglia profoundly influenced the course of synaptic sprouting. While microglial contacts can
647 facilitate spine formation of functional synapses both during development and in adult stages
648 (Miyamoto et al., 2013, 2016; Wake et al., 2009; Weinhard et al., 2018; Y. Wu et al., 2015) the extent
649 and speed of microglia-mediated effects in *ex vivo* brain slices was surprising. Thus, further studies will
650 be required to reveal the molecular mechanisms underlying these effects, potentially making the acute
651 slice maturation process a valuable model for studying microglia-synapse interactions.

652 To our knowledge, we show for the first time that the presence of functional microglia can
653 actively influence SWR activity in hippocampal acute slice preparations, which was largely mediated
654 by purinergic mechanisms. Thus, the presence of microglia and functional P2Y12R signalling are
655 required for the emergence of physiological-like network activity in *ex vivo* slices suggesting that

interventions aiming to inhibit microglial actions could render acute brain slices less capable of producing normal patterns of neuronal network activity seen *in vivo*. Previously it has been demonstrated that hippocampal field excitatory postsynaptic potentials (fEPSPs) recover in correlation with synaptic changes in *ex vivo* slices (Kirov et al., 1999). Our results show that SWR activity shows a huge increase in amplitude, rate and frequency when correlated to the measured synaptic density changes. Since the generation of SWRs in these conditions are both reliant on a sufficiently large tonic excitatory activity and the action of reciprocally connected parvalbumin positive basket cells (Schlingloff et al., 2014), these results indicate that a delicate balance needs to be maintained between excitation and inhibition during the course of sprouting which allows SWRs to emerge. Importantly, our results showed that microglia can facilitate glutamatergic and repress GABAergic synaptic formation to maintain a balanced reorganization of the network after the loss of synapses due to the slice preparation procedure. Supporting our data, partial depletion of microglia promoted asynchronous activity without overall change in frequency (Akiyoshi et al., 2018), while microglia depletion in the hippocampus decreased spontaneous and evoked glutamatergic activity (Basilico et al., 2022). In contrast, *in vivo* imaging experiments showed increased excitatory and inhibitory neuronal activity in the cortex after microglia depletion, which results are in line with *ex vivo* circuit mapping data (Császár et al., 2022; Liu et al., 2021, 2022). Thus, it is likely that in addition to the synaptic density changes, the altered distribution, morphology, and subsequent changes in microglia-neuron interactions are also key players in maintaining the integrity of neuronal networks in *ex vivo* acute slices, enabling complex, *in vivo*-like network activity patterns to emerge.

Acute slice preparation is a well-established experimental approach, which is extremely useful to study the physiology of neurons and other cells from individual synapses to complex neuronal networks. However, precautions are necessary during the interpretation of results, as certain changes in these conditions may reflect different physiological or pathological states concerning both neuronal and microglial functions. In fact, we show that microglia in acute slices can present a rapid transition into a more reactive phenotype and can actively influence the neuronal network through interactions via altered microglia-neuron interactions and purinergic signalling. Since microglial morphology strongly reflects the state of the tissue, we suggest that monitoring these changes should always be considered,

as it could help in the contextualization of results concerning both the microglial and neuronal populations. Moreover, an extensive examination and comparison of microglial phenotype state changes due to different slice preparation methods could facilitate more refined and consistent experimental models and paradigms to be established. In addition, our results also emphasize the importance of interactions between microglia and complex neuronal networks, which may be further emphasized by the sensitivity of microglia to a broad range of changes in their micro- and macroenvironment. While the observed changes in microglia in acute slices may not represent an undisturbed physiological state, the acute slice model also emerges as an instrumental tool to test and understand the different factors, which contribute to reactive microglial phenotypes, with broad implications for diseases of the CNS that are influenced by alterations of microglial function.

Materials & Methods

Animals

In all experiments, CX3CR1$^{+/GFP}$ or C57Bl/6J mice littermates of both sexes were used. Mice were kept in the vivarium on a 12-hour light/dark cycle and provided with food and water ad libitum. The animals were housed two or three per cage. All experiments were approved by the Ethical Committee for Animal Research at the Institute of Experimental Medicine, Hungarian Academy of Sciences, and conformed to Hungarian (1998/XXVIII Law on Animal Welfare) and European Communities Council Directive recommendations for the care and use of laboratory animals (2010/63/EU) (license number PE/EA/2552-6/2016; PE/EA/254-7/2019).

Slice preparation, incubation and fixation

In order to minimize bacterial contamination, all the tools and containers used for slice preparation and incubation were routinely cleaned before and after experiments with 70% ethanol and were rinsed extensively with distilled water. For acute slice preparation, mice were decapitated under deep isoflurane anesthesia. The brain was removed and placed into an ice-cold cutting solution, which had been bubbled with *95% O2–5% CO2* (carbogen gas) for at least 30 min before use. The cutting solution contained the following (in mM): *205 sucrose, 2.5 KCl, 26 NaHCO3, 0.5 CaCl2, 5 MgCl2, 1.25 NaH2PO4, 10 glucose*, saturated with *95% O2–5% CO2*. Horizontal hippocampal slices of 300 µm or 450 µm (in case of LFP recordings) thickness were cut using a Vibratome (Leica VT1000S). The process of slice preparation from termination till the first slice to be immersion-fixed took ~5-10 minutes.

After acute slice preparation, slices were placed into an interface-type holding chamber for recovery. In an interface-type chamber, slices are laid onto a mesh just slightly submerged into the artificial cerebrospinal fluid (ACSF), therefore the oxygenation of the tissue is mainly realized by the direct exposure to humidified oxygen-rich air above the slices. This chamber contained standard ACSF at 35°C that gradually cooled down to room temperature. The ACSF solution contained the following (in mM): *126 NaCl, 2.5 KCl, 26 NaHCO3, 2 CaCl2, 2 MgCl2, 1.25 NaH2PO4, 10 glucose*, saturated with *95% O2–5% CO2*. Immediately after slice preparation/given timeframes of incubation/after recordings, slices were immersion-fixed for 1 hour with 4% PFA solution. In the case of PSB treated acute slices, both cutting and standard ACSF solutions used to prepare the slices contained 10 µM PSB-0739 (Sigma-Aldrich).

For perfusion-fixed slices, mice were anesthetized and transcardially perfused with 0.9% NaCl solution for 1 minute, followed by 4% PFA in 0.1 M phosphate buffer (PB) for 40 minutes, followed by 0.1 M PB for 10 minutes to wash the fixative out. Blocks containing the somatosensory cortex and ventral hippocampus were dissected, and horizontal sections were prepared on a vibratome (VT1200S, Leica, Germany) at 50 µm thickness for immunofluorescent histological and 100 µm thickness for the automated morphological analysis.

Lab#2 slice preparation protocol:

Mice were anesthetized with isoflurane and decapitated according to a protocol approved by the UCLA Chancellor's Animal Research Committee. After decapitation the head was immersed in ice-cold ACSF solution (see below) and put in the -80°C freezer for 1 minute. The brain was then removed from the skull and coronal 350 µm thick slices were cut from a range of AP (from bregma): - 0.5 to -3 mm on a Leica VT1000S vibratome in ice-cold N-Methyl-D-Glutamine (NMDG)-based HEPES-buffered solution, containing (in mM): 135 NMDG, 10 D-glucose, 4 MgCl2, 0.5 CaCl2, 1 KCl, 1.2 KH2PO4, 20 HEPES, 27 sucrose (bubbled with 100% O2, pH 7.4, 290-300 mOsm/L). Then, slices were incubated at 34°C in a reduced sodium + sucrose artificial CSF (ACSF), containing (in mM): NaCl 85, D-glucose 25, sucrose 55, KCl 2.5, NaH2PO4 1.25, CaCl2 0.5, MgCl2 4, NaHCO3 26, pH 7.3-7.4 when bubbled with 95% O2, 5% CO2 before fixation. Each slice was placed with the same orientation into an incubation chamber, and the slice surface was identified as the side facing towards the top. The incubation period for a series of slices from the same animal was designed as: 0 minutes (this slice was also placed into the incubation chamber for 3-5 seconds), 20 minutes, 1 hour, 2 hours and 5 hours. After a certain time of incubation, the corresponding slice was carefully transferred from the incubation chamber to a 24 well plate pre-filled with 4% freshly depolimerized paraformaldehyde in 0.1 M phosphate buffer (PFA) for fixation. Each slice spent exactly 1 hour in fixative before transferring into the “wash” plate and washed extensively with 0.1 PBS by exchanging the PBS in the well 3 times first, then placing the washing plate on a shaker and washing in PBS for 3x10 minutes. Slices were then

751 individually inserted into 15 ml plastic test-tubes sandwiched between tissue paper to avoid shaking
752 during transportation. The test-tubes were placed in a Styrofoam container and shipped to the IEM.
753
754 **Lab#3 slice preparation protocol:**
755 C57Bl/6J mice at the age of 4 weeks were decapitated under deep isoflurane anesthesia. The
756 brain was quickly removed and immersed in ice-cold sucrose-containing artificial cerebrospinal fluid,
757 saturated with 95% O2- 5% CO2 (sucrose-containing ACSF; in mM: NaCl 60, sucrose 100, KCl 2.5,
758 NaH2PO4 1.25, NaHCO3 26, CaCl2 1, MgCl2 5, D-glucose 20; pH 7.4, 310 mOsmol). Coronal
759 hippocampal slices (300 µm thick) were prepared with a vibratome (VT1200S, Leica). The slices were
760 incubated at 35°C in the same solution for 20 min. The 0-minute slice was placed into the incubation
761 chamber for a few seconds (3-5 seconds) before fixation with 4% PFA. Then, 20 minutes slices were
762 fixed with 4% PFA before being transferred to second chamber filled with ACSF saturated with 95%
763 O2- 5% CO2 at room temperature (ACSF; in mM: NaCl 125, KCl 3.5, NaH2PO4 120, NaHCO3 26,
764 CaCl2 2, MgCl2 5, D-glucose 15; pH 7.4, 310 mOsmol). After that, 1 hour, 2 hours and 5 hours slices
765 were fixed with 4% PFA. Each slice spent 1 hour for fixation, and then transferred into wash plates
766 containing 0.1 M phosphate buffer (PB) and washed with PB 3 times for 10 minutes. All slices were
767 stored and transported submerged under 0.1 M PB, supplemented with 0.05 % sodium-azide.

768 ***Cross section of slice preparations and quantification of translocation***
769 300 µm thick acute slices were immersion fixed immediately after slicing (0 minute) or after
770 20 minutes, 1 hour, 2 hours or 5 hours spent in an interface-type incubation chamber (Fig 1A). Fixed
771 slices were washed in 0.1M PB, flat embedded in 2% agarose blocks, rotated 90 degrees, and resliced
772 on a vibratome (VT1200S, Leica, Germany) at 50 µm thickness (Fig 1B). The sections were mounted
773 on glass slides, and coverslipped with Aqua-Poly/Mount (Polysciences). Intrinsic ($CX3CR1^{+/GFP}$)
774 immunofluorescence was analyzed using a Nikon Eclipse Ti-E inverted microscope (Nikon Instruments
775 Europe B.V., Amsterdam, The Netherlands), with a CFI Plan Apochromat VC 20X DIC N2 objective
776 (numerical aperture: 075) and an A1R laser confocal system. We used 488 nm excitation laser (CVI
777 Melles Griot), and image stacks (resolution: 0.62 µm/px) were taken with NIS-Elements AR. Maximal
778 intensity projections of stacks containing the whole section thickness were saved in tiff format, cell
779 bodies were masked with Fiji "Analyze particles" plugin. Cell-body masks were used to count cells,
780 and these masks were subtracted from the original tiff files to get images containing microglial
781 processes only. As a validation for volume-related quantifications in acute slices, the average thickness
782 for each preparation across the incubation procedure was measured (mean±SD: 262±7 µm), which
783 showed no substantial differences between groups (Kruskal-Wallis test, $p>0.05$). For quantification, a
784 measuring grid was placed onto the entire thickness of cross-sections (Fig 1 C), which divided the
785 thickness into 7 equal zones. Cell body numbers were counted within these grids, and microglial process
786 volume was assessed by measuring fluorescent integrated density within the grids with Fiji software.

787 Cell-body translocation calculation (Fig 1F) was performed for assessing microglial movement towards
788 the top surface, and for away from the middle Z-depth of the slices. The coordinates for cell bodies
789 were registered in Fiji software, the distance of the cell bodies from the bottom surface or the (middle
790 Z-depth) were measured at 0 min, and at 5 hours (the number of measured cells was identical at the two
791 time-points). The distances were sorted in growing rows for both timepoints, and the 0-minute values
792 subtracted from the 5-hour values, thus we could calculate the minimal values cells had to travel in
793 order to reach the final distribution pattern (at 5 hours) starting from the 0 minutes distribution. For the
794 process area coverage measurement (Fig 1I) the images with cell bodies masked out were used. Images
795 from slices fixed at 0 minutes and 5 hours were binarized in Fiji, and the percentage of covered area
796 measured.

797 ***Time-lapse imaging***

798 Acute brain slices (300µm thick) were prepared from 80-day old CX3CR1$^{+/GFP}$ mice as described above.
799 Z-stack images (1µm step size) were acquired using a Nikon C2 laser scanning confocal microscope
800 equipped with a 20x CFI Plan Apo VC (NA=0.75 WD=1.00mm FOV=1290.4mm) objective at 488nm,
801 under continuous perfusion with ACSF (3 ml/min perfusion rate). The image acquisition started 1h after
802 slice cutting. Image stacks were taken every 20 min for 6 hours. Video editing was performed using
803 NIS Elements 5.00 and ImageJ 1.53f51.

804 ***Automated morphological analysis of microglial cells***

805 300 µm thick acute slices were immersion fixed for 1 hour immediately after slicing (0 minute)
806 or after 20 minutes, 1 hour, 2 hours or 5 hours spent in an interface-type incubation chamber (Fig 1A).
807 Fixed slices were washed in 0.1M PB, flat embedded in 2% agarose blocks, and re-sectioned on a
808 vibratome (VT1200S, Leica, Germany) at 100 µm thickness (Fig 1B). Sections selected from the middle
809 region of incubated slices were immunostained with antibodies, and DAPI (for primary and secondary
810 antibodies used in this study, please see Table 1.). Preparations were kept in free-floating state until
811 imaging to minimize deformation of tissue due to the mounting process. Imaging was carried out in
812 0.1M PB, using a Nikon Eclipse Ti-E inverted microscope (Nikon Instruments Europe B.V.,
813 Amsterdam, The Netherlands), with a CFI Plan Apochromat VC 60X water immersion objective
814 (numerical aperture: 1.2) and an A1R laser confocal system. Volumes were recorded with 0.2 µm/pixel
815 resolution and a Z-step of 0.4µm. For 3-dimensional morphological analysis of microglial cells, the
816 open-source MATLAB-based Microglia Morphology Quantification Tool was used (available at
817 https://github.com/isdneuroimaging/mmqt). This method uses microglia and cell nuclei labeling to
818 identify microglial cells. Briefly, 59 possible parameters describing microglial morphology are
819 determined through the following automated steps: identification of microglia (nucleus, soma,

branches) and background, creation of 3D skeletons, watershed segmentation and segregation of individual cells (Heindl et al., 2018).

Primary antibodies	host	source	catalog nr.	RRID
Gephyrin	Mouse	Synaptic Systems	147 021	AB_2232546
GFP	Chicken	Invitrogen	A10262	AB_2534023
Homer1	Rabbit	Synaptic Systems	160 003	AB_887730
IBA1	Guinea pig	Synaptic Systems	234004	AB_2493179
Kv2.1	Mouse	NeuroMab	75-014	AB_10673392
P2Y12R	Rabbit	Anaspec	AS-55043A	AB_2298886
TMEM119	Chicken	Synaptic Systems	400 006	AB_2744643
vGAT	Guinea pig	Synaptic Systems	131 004	AB_887873
VGLUT1	Guinea pig	Synaptic Systems	135 304	AB_887878
Secondary antibodies	**host**	**source**	**catalog nr.**	**RRID**
Alexa 488 Streptavidin	-	-	S-11223	-
Alexa 488 anti-chicken	donkey	Jackson ImmunoResearch Labs	703-546-155	AB_2340376
Alexa 488 anti-guinea-pig	donkey	Jackson ImmunoResearch Labs	706-546-148	AB_2340473
Alexa 488 anti-guinea-pig	donkey	Jackson ImmunoResearch Labs	706-546-148	AB_2340473
Alexa 488 anti-mouse	donkey	Thermo Fisher Scientific	A-21202	AB_141607
Alexa 488 anti-rabbit	donkey	Jackson	711-546-152	AB_2340619
Alexa 594 anti-guinea-pig	goat	LifeTech	A11076	AB_141930
Alexa 594 anti-mouse	donkey	Invitrogen	A-21203	AB_141633
Alexa 594 anti-rabbit	donkey	LifeTech	A21207	AB_141637
Alexa 647 anti-chicken	donkey	Jackson ImmunoResearch Labs	703-606-155	AB_2340380
Alexa 647 anti-rabbit	donkey	Jackson ImmunoResearch Labs	711-605-152	AB_2492288
Alexa 647anti-guinnea-pig	donkey	Jackson ImmunoResearch Labs	706-606-148	AB_2340477
Biotinylated anti-chicken	goat	Vector Laboratories	BA-9010	AB_2336114

Table 1. List of antibodies used in the study.

822 ***Pre-embedding immunofluorescent labelling and analysis of CLSM data***

823 Before the immunofluorescent labelling, the 50 µm thick sections were washed in PB and Tris-
824 buffered saline (TBS). Thorough washing was followed by blocking for 1 hour in 1% human serum
825 albumin (HSA; Sigma-Aldrich) and 0.03-0.1% Triton X-100 dissolved in TBS. After this, sections were
826 incubated in mixtures of primary antibodies, diluted in TBS overnight at room temperature. After
827 incubation, sections were washed in TBS and were incubated overnight at 4 °C in the mixture of
828 secondary antibodies, all diluted in TBS. Secondary antibody incubation was followed by washes in
829 TBS, PB, the sections were mounted on glass slides, and coverslipped with Aqua-Poly/Mount
830 (Polysciences). Immunofluorescence was analyzed using a Nikon Eclipse Ti-E inverted microscope
831 (Nikon Instruments Europe B.V., Amsterdam, The Netherlands), with a CFI Plan Apochromat VC 60X
832 oil immersion objective (numerical aperture: 1.4) and an A1R laser confocal system. We used 405, 488,
833 561 and 647 nm lasers (CVI Melles Griot), and scanning was done in line serial mode, pixel size was
834 50x50 nm. Image stacks were taken with NIS-Elements AR. For primary and secondary antibodies used
835 in this study, please see Table 1. Quantitative analysis of each dataset was performed by at least two
836 observers, who were blinded to the origin of the samples, the experiments, and did not know of each
837 other's results.

838 For the analysis of somatic contact prevalence, confocal stacks with double immunofluorescent
839 labeling (cell type-marker and microglia) were acquired from at least three different regions of mouse
840 cortex. All labeled and identified cells were counted when the whole cell body was located within the
841 Z-stack. Given somata were considered to be contacted by microglia, when a microglial process clearly
842 touched it (i.e., there was no space between neuronal soma and microglial process) on at least 0.5 µm
843 long segment.

844 Microglial process coverage was measured on CLSM Z-stacks acquired with a step size of 300 nm. On
845 single-channel images, Kv2.1-positive cells were selected randomly, the cell bodies of which were fully
846 included in the captured volume. The surface of these cells was calculated by measuring the
847 circumference of the soma on every section multiplied by section thickness. The surface of microglial
848 process contacts was measured likewise.

849 For the analysis of synaptic contact prevalence, confocal stacks with triple immunofluorescent
850 labeling (pre- and postsynaptic markers and microglia) were analyzed using an unbiased, semi-
851 automatic method. First, the two channels representing the pre- and postsynaptic markers were exported
852 from a single image plane. The threshold for channels were set automatically in FIJI, the „fill in holes"
853 and „erode" binary processes were applied. After automatic particle tracking, synapses were identified
854 where presynaptic puncta touched postsynaptic ones. From these identified points we selected a subset
855 in a systematic random manner. After this, the corresponding synapses were found again in the original
856 Z-stacks. A synapse was considered to be contacted by microglia, when a microglial process was closer
857 than 200 nm (4 pixels on the images).

858 ***Post-embedding immunofluorescent labelling and quantitative analysis***

859 The technique described by Holderith et al. (Holderith et al., 2021.) was used with slight
860 modifications. 300 µm thick acute slices were cut from CX3CR1$^{+/GFP}$ mouse line and then immersion
861 fixed immediately after slicing (0 minute) or after 20 minutes, 1 hour, 2 hours or 5 hours spent in an
862 interface-type incubation chamber (Fig 1 B). Fixed slices were washed in 0.1M PB and 0.1M Maleate
863 Buffer (MB, pH: 6.0). Then slices were treated with 1% uranyl-acetate diluted in 0.1M MB for 40
864 minutes in dark. This was followed by several washes in 0.1M PB, then slices were dehydrated in
865 ascending alcohol series, acetonitrile and finally embedded in Durcupan (Fluca). Each block contained
866 all slices from a respective time series of one animal. Ultrathin sections were cut using a Leica UC7
867 ultramicrotome at 200 nm thickness and collected onto Superfrost Ultra plus slides and left on a hotplate
868 at 80°C for 30 minutes then in oven at 80°C overnight (Fig 3 C). Sections were encircled with silicon
869 polymer (Body Double standard kit, Smooth-On, Inc.) to keep incubating solutions on the slides. The
870 resin was etched with saturated Na-ethanolate for 5 minutes at room temperature. Then sections were
871 rinsed three times with absolute ethanol, followed by 70% ethanol and then DW. Retrieval of the
872 proteins were carried out in 0.02M Tris Base (pH = 9) containing 0.5% sodium dodecyl sulfate (SDS)
873 at 80°C for 80 min. After several washes in TBS containing 0.1% Triton X-100 (TBST, pH = 7.6),
874 sections were blocked in TBST containing 6% BlottoA (Santa Cruz Biotechnology), 10% normal goat
875 serum (NGS, Vector Laboratories) and 1% BSA (Sigma) for 1 hour then incubated in the primary Abs
876 diluted in blocking solution at room temperature overnight with gentle agitation. After several washes
877 in TBST the secondary Abs were applied in TBST containing 25% of blocking solution for 3 hours.
878 After several washes in TBST, slides were rinsed in DW then sections were mounted in Slowfade
879 Diamond (Invitrogen) and coverslipped. Immunofluorescence was analyzed using a Nikon Eclipse Ti-
880 E inverted microscope (Nikon Instruments Europe B.V., Amsterdam, The Netherlands), with a CFI
881 Plan Apochromat VC 60X oil immersion objective (numerical aperture: 1.4) and an A1R laser confocal
882 system. We used 488 and 647 nm lasers (CVI Melles Griot), and scanning was done in line serial mode,
883 pixel size was 50x50 nm. Image stacks were taken with NIS-Elements AR. For primary and secondary
884 antibodies used in this study, please see Table 1. Quantitative analysis of each dataset was performed
885 by at least two observers, who were blinded to the origin of the samples, the experiments, and did not
886 know of each other's results.

887 For the quantitative assessment of P2Y12R expression, single high-resolution CLSM image
888 planes were used. Microglial cell bodies, thick (average diameter greater than 1 µm) and thin (average
889 diameter less than 1 µm) processes were identified based on TMEM119 and CX3CR1$^{+/GFP}$ staining.
890 Once the respective outlines of these profiles have been delineated, these outlines have been extended
891 both in the intra- and the extracellular direction with 250-250 nm, yielding a 500 nm wide ribbon-
892 shaped ROI. The integrated fluorescent density of P2Y12R-labeling was measured and divided by the

893 lengths of the respective ROIs, which gave us the P2Y12R fluorescent intensity values applied to unit
894 membrane lengths for each profile.
895 For the synapse density measurements, we used double stainings for pre- and postsynaptic
896 markers (vGluT1 with Homer1 for glutamatergic, and vGAT with Gephyrin for GABAergic synapses).
897 We could validate the specificity and sensitivity of these stainings based on the near-perfect match
898 between pre and postsynaptic markers, thus we continued to measure the presynaptic signals. ROIs
899 were randomly chosen within the neuropil, avoiding cell bodies. The integrated fluorescent densities
900 were measured within these ROIs for vGluT1 and vGAT channels. Measurements were performed with
901 the Fiji software package.

902 ***Ex vivo 2-photon imaging of extracellular ATP***

903 For extracellular expression of the ATP sensor $GRAB_{ATP}$ in neurons,
904 Vglut1/cre/Gt(Rosa26)Sor[cre/cre] mice(ref) were crossed with LSL_$GRAB_{ATP}$_P2A_jRGECO1a
905 (TgTm) - C57Bl/6J [flox/flox] mice made by Biocytogen (China). Mice were used in the *ex vivo* 2-
906 photon imaging experiments at the age of 67-72 days. Acute slices were obtained as in previous
907 experiments (Methods/Slice preparation and incubation). Slices including the hippocampus and cortical
908 regions above were used for two photon imaging (5 slices/brain). The slices were split and from each
909 plane one half was used for imaging within the CA3 area in the hippocampus and the other half for
910 imaging within layer two in the cortex, both in a 256*128 um window. The time between slice cutting
911 and imaging was minimized to 8-13 min for the very first slices. For each slice, 10 min imaging at 0.5
912 frame/sec rate was followed by Z-stack acquisition (3 um step size; taking ~3-4 min, see experimental
913 setup on Fig 5A). Two photon imaging was accomplished by a Nikon Eclipse FN1 upright microscope,
914 equipped with a Nikon A1R MP+ multiphoton system using a Chameleon Vision II Ti: Sapphire tunable
915 (680-1080 nm) laser and a 25x water dipping objective lens [CFI75 Apo LWD NA=1.1 WD=2 mm].
916 The excitation wavelength was set to 920 nm for detecting the signal and 550/88 nm emission filter and
917 a GaAsP NDD PMTs detector was used. Time lapse data were analyzed using the NIS-Elements
918 (version 5.42.02) and ImageJ (version 1.53t) software. Mean fluorescent intensity (MFI) decreases (Fig
919 5B-C) were measured in areas where no ATP flash activity (focal ATP surges) was observed [ROI size:
920 12,5*12,5 um; 4 ROI/slice]. Z-stack images were used to determine the fluorescent signal decrease in
921 time and depth (Fig 5D-E, Suppl Fig 2C), by averaging MFI data from 3 regions [ROI size: 25*50um]
922 from each slice. ATP flashes were identified on each slice manually, encircling the individual flashes
923 when the signal intensity was at maximum. Then, flash size, mean fluorescent intensity, peak duration,
924 rise time and decay time data were collected and analyzed. Details of statistical analysis are provided
925 in Fig 5 legend and Suppl Fig 3.
926

927 ***Selective depletion of microglia***

928 CX3CR1$^{+/GFP}$ or C57B1/6J littermates were subjected to 3 weeks of either control or PLX3397
929 containing diet to create control and microglia depleted subgroup of animals, respectively. Extra slices
930 were gathered from each animal by the re-slicing of immersion-fixed or perfusion-fixed acute slice
931 preparations (50 µm). Success of depletion was monitored by creating z-stack images of the native GFP
932 signal of microglia with confocal laser-scanning microscopy and verified by comparing the total
933 number of microglia counted (via Fiji counting tool) at the same cortical and hippocampal locations,
934 and through the whole depth of the slice preparations.

935 ***Patch clamp recordings***

936 Generally accepted guidelines were followed for patching microglial cells (Avignone et al.,
937 2019). After incubation for given timeframes (as specified for each experiment in the Results section),
938 slices were transferred individually into a submerged-type recording chamber with a superfusion system
939 allowing constantly bubbled (95% O2–5% CO2) ACSF to flow at a rate of 3-3.5 ml/min. The ACSF
940 was adjusted to 300-305 mOsm and was constantly saturated with 95% O2–5% CO2 during
941 measurements. All measurements were carried out at 33 –34°C, temperature of ACSF solution was
942 maintained by a dual flow heater (Supertech Instruments). The pipette solution contained (in mM): 120
943 KCl, 1 CaCl2, 2 MgCl2, 10 HEPES, and 11 EGTA, pH: 7.3, 280-300 mOsm. Pipette resistances were
944 3-6 MΩ when filled with pipette solution. Visualization of slices and selection of cells (guided by native
945 GFP signal) was done under an upright microscope (BX61WI; Olympus, Tokyo, Japan equipped with
946 infrared-differential interference contrast optics and a UV lamp). Only cells located deeper than ~50
947 µm measured from the slice surface were targeted. All cells were initially in voltage-clamp mode and
948 held at -40 mV holding potential during the formation of the gigaseal. Series resistance was constantly
949 monitored after the whole-cell configuration was established, and individual recordings taken for
950 analysis showed stability in series resistance between a 5% margin during the whole recording. After
951 whole-cell configuration was established, resting membrane potential values were measured by
952 changing the recording configuration to current-clamp mode at 0 pA for a short period of time (10-15
953 seconds) and evaluated from the recorded signal via averaging a 5 second period. Thereafter, responses
954 to a pulse-train of current steps (-2 pA to -10 pA with 2 pA increments and 10 ms duration) were
955 recorded. Quantification of input resistance of cells was derived via Ohm's law based on the slope of
956 voltage responses measured at each current step. The inter-pulse interval was 100 ms. Recordings were
957 performed with a Multiclamp 700B amplifier (Molecular Devices). Data were digitized at 10 kHz with
958 a DAQ board (National Instruments, USB-6353) and recorded with a custom software developed in
959 C#.NET and VB.NET in the laboratory. Analysis was done using custom software developed in Delphi
960 and Python environments.

961 ***LFP Recordings***

962 Acute slice preparations were gathered at each recording day (6 slices/animal, 450 µm thick)
963 in a pairwise manner from control and microglia depleted animals while using the same solutions and
964 equipment. The slice preparation sequence was alternated throughout the recording days between the
965 two groups, as well as the chambers that were used for the incubation process, to minimize artefacts
966 that might have been introduced by variance in slice preparation or incubation quality. After at least 1
967 hour of incubation, slices from both conditions were transferred together in a pairwise manner to a dual
968 perfusion system recording chamber (Hájos and Mody, 2009), and measured simultaneously via
969 performing local field potential (LFP) recordings. In this design, the slices were placed on a metal mesh,
970 and two separate fluid inlets allowed ACSF to flow both above and below the slices at a rate of 3–3.5
971 ml/min for each flow channel at 33 –34°C (Supertech Instruments). The position of slices from the two
972 conditions were also alternated in the recording chamber between subsequent measurements. Standard
973 patch pipettes filled with ACSF were used for LFP recordings. Recording pipettes were positioned at
974 the same depth (~80-100 µm below the surface) and in the same region (pyramidal layer of CA3) in
975 both conditions. ACSF containing pipette resistances were 3–6 MΩ. Recordings were performed with
976 a Multiclamp 700B amplifier (Molecular Devices). Data were digitized at 10 kHz with a DAQ board
977 (National Instruments, USB-6353) and recorded with software developed in C#.NET and VB.NET in
978 the laboratory.

979 ***Digital signal processing and analysis***

980 All data were processed and analyzed off-line using self-developed programs written in Delphi 6.0 by
981 A.I.G. and Python 2.7.0 by D.S. Signals were filtered with a two-way RC filter to reserve phase. SWRs
982 were pre-detected on 30 Hz low-pass-filtered field recordings using a threshold value of 2-3 times the
983 SD of the signal. Recordings were considered to not contain SWRs if 2 times the SD of the signal did
984 not result in detectable events. All automatic detection steps were supervised in each recording. The
985 predetected SWRs were then analyzed using a program that measured various SWR features and
986 eliminates recording artefacts similar to SWRs. Namely, on the low-pass-filtered signal, the program
987 measured: peak amplitude of sharp waves (SWR amplitude); inter- sharp wave interval (SWR rate). On
988 a ripple bandpass-filtered trace (200 ±30 Hz), the program also detected the time of negative ripple
989 peaks. Based on this, we identified the ripple cycle closest to the SWR peak and used its negative peak
990 as triggering event for averages to preserve ripple phase. Taking the absolute value of the ripple
991 bandpassed signal and low pass filtering it, we calculated the ripple power peak (Ripple amplitude).
992 After detection, ~100 consecutive events were selected for quantification, where highest values were
993 measured along the whole recording.

994 ***Quantification and statistical analysis***

995 All quantitative assessments were performed in a blind manner. Sample size was determined
996 based on sample size calculations performed in our previous experiments using similar models. Data
997 were sampled in a systematic random manner. Experiments were replicated by using multiple animals
998 for slice preparations or histology (biological replicates), and pooled results from experiments were
999 presented in the Figs. Exclusion criteria were pre-established for quality of acute slices and
1000 immunostainings. No samples had been excluded in the present paper. Normality of the data was tested
1001 via Shapiro-Wilk test, to decide whether to use parametric or non-parametric tests during further
1002 analysis. In the case of two independent groups, Student's t-test, or Mann-Whitney U-test, for three or
1003 more independent groups Kruskal-Wallis test with Dunn's multiple comparison test was applied.
1004 Statistical tests were conducted in custom or self-developed programs in Python environment 2.7.0 by
1005 D.S. In this study, data are presented as mean±SEM or in median-Q1-Q3 format, $p<0.05$ was considered
1006 statistically significant.

1007 # Acknowledgements

1008 We thank László Barna, Pál Vági and the Nikon Imaging Center at the Institute of Experimental Medicine (IEM)
1009 for kindly providing microscopy support. We thank Zsolt Kohus for methodological concepts and preliminary
1010 electrophysiological data. We are also grateful to Norbert Hájos (IEM), Zoltán Nusser (IEM), and Dániel
1011 Schlingloff (IEM) for their support and useful comments.

1012 # Author contributions

1013 Experimental design and overall concept, A.D., C.C., A.G., P.B.; Methodology, C.C., P.B., B.P., Z.K., E.S., H.B.,
1014 K.A., I.M., X.W., K.H., Y.W., Z.W., M.J., Y.L; Formal Analysis C.C., P.B., B.P., Z.K.; Investigation, P.B., C.C.,
1015 B.P., E.S., Z.K., A.K., M.N; Resources, A.D., A.G. Writing – Original Draft, P.B., C.C., A.D., Z.K.; Editing, P.B.,
1016 C.C., B.P., A.D., Z.K., H.B., K.A. I.M., X.W.; Visualization P.B., C.C., B.P., Z.K. Supervision A.D. and A.G.;
1017 Project Administration A.D.; Funding Acquisition, A.D.

1018 # Author ORCIDs

1019 Péter Berki: 0000-0001-9550-433X; Csaba Cserép: 0000-0001-5513-2471; Balázs Pósfai: 0000-0003-1035-
1020 565X; Eszter Szabadits: 0000-0003-4271-2009; Zsuzsanna Környei: 0000-0001-8281-7994; Anna Kellermayer:
1021 0000-0001-5241-7009; Miklós Nyerges: 0000-0001-5044-6439; Xiaofei Wei: 0000-0002-1173-4734; Istvan
1022 Mody: 0000-0002-7975-7959; Kunihiko Araki: 0000-0002-0859-7046; Heinz Beck: 0000-0002-8961-998X;
1023 Zhaofa Wu: 0000-0003-2027-5194; Miao Jing: 0000-0002-7782-5065; Yulong Li: 0000-0002-9166-9919; Attila
1024 I. Gulyás: 0000-0003-4961-636X; Ádám Dénes: 0000-0001-6919-4905.

1025 # Competing interests

1026 The authors declare no competing interests.

1027 # Ethics statement

1028 All experiments were approved by the Ethical Committee for Animal Research at the Institute of Experimental
1029 Medicine, Hungarian Academy of Sciences, and conformed to Hungarian (1998/XXVIII Law on Animal Welfare)
1030 and European Communities Council Directive recommendations for the care and use of laboratory animals
1031 (2010/63/EU) (license number PE/EA/2552-6/2016; PE/EA/254-7/2019).

Funding

This work was supported by „Momentum" research grant from the Hungarian Academy of Sciences (LP2016-4/2016, and LP2022-5/2022 to A.D.) ERC-CoG 724994 (to A.D.) and Hungarian Brain Research Program NAP2022-I-1/2022 a (to A.D.). and Hungary-China Intergovernmental Science and Technology Innovative Cooperation project (2021YFE0116400 to M.J. and 2020-1.2.4-TÉT-IPARI-2021-00005 to A.D.). C. C. was supported by the János Bolyai Research Scholarship of the Hungarian Academy of Sciences. C. C. (UNKP-22-5) and B. P. (UNKP-22-4-I) were supported by the New National Excellence Program of the Ministry for Innovation and Technology. I.M. was supported by the National Institutes of Health/National Institute of Aging grant R01050474 and the Coelho Endowment. H.B. was supported by SFB 1089 and EXC 2151 under Germanys Excellence Strategy, both of the Deutsche Forschungsgemeinschaft (DFG, German Research Foundation).

References

Akiyoshi, R., Wake, H., Kato, D., Horiuchi, H., Ono, R., Ikegami, A., Haruwaka, K., Omori, T., Tachibana, Y., Moorhouse, A. J., & Nabekura, J. (2018). Microglia Enhance Synapse Activity to Promote Local Network Synchronization. *ENeuro*, *5*(5), ENEURO.0088-18.2018. https://doi.org/10.1523/ENEURO.0088-18.2018

Andersen, P. (1981). Brain slices—A neurobiological tool of increasing usefulness. *Trends in Neurosciences*, *4*, 53–56. https://doi.org/10.1016/0166-2236(81)90019-9

Avignone, E., Milior, G., Arnoux, I., & Audinat, E. (2019). *Electrophysiological Investigation of Microglia* (Vol. 2034, p. 111). Springer. https://doi.org/10.1007/978-1-4939-9658-2_9

Basilico, B., Ferrucci, L., Ratano, P., Golia, M. T., Grimaldi, A., Rosito, M., Ferretti, V., Reverte, I., Sanchini, C., Marrone, M. C., Giubettini, M., De Turris, V., Salerno, D., Garofalo, S., St-Pierre, M.-K., Carrier, M., Renzi, M., Pagani, F., Modi, B., … Ragozzino, D. (2022). Microglia control glutamatergic synapses in the adult mouse hippocampus. *Glia*, *70*(1), 173–195. https://doi.org/10.1002/glia.24101

Bennett, F. C., Bennett, M. L., Yaqoob, F., Mulinyawe, S. B., Grant, G. A., Hayden Gephart, M., Plowey, E. D., & Barres, B. A. (2018). A Combination of Ontogeny and CNS Environment Establishes Microglial Identity. *Neuron*, *98*(6), 1170-1183.e8. https://doi.org/10.1016/j.neuron.2018.05.014

Bisht, K., Okojie, K. A., Sharma, K., Lentferink, D. H., Sun, Y.-Y., Chen, H.-R., Uweru, J. O., Amancherla, S., Calcuttawala, Z., Campos-Salazar, A. B., Corliss, B., Jabbour, L., Benderoth, J., Friestad, B., Mills, W. A., Isakson, B. E., Tremblay, M.-È., Kuan, C.-Y., & Eyo, U. B. (2021). Capillary-associated microglia regulate vascular structure and function through PANX1-P2RY12 coupling in mice. *Nature Communications*, *12*(1), Article 1. https://doi.org/10.1038/s41467-021-25590-8

Bohlen, C. J., Bennett, F. C., Tucker, A. F., Collins, H. Y., Mulinyawe, S. B., & Barres, B. A. (2017). Diverse Requirements for Microglial Survival, Specification, and Function Revealed by Defined-Medium Cultures. *Neuron*, *94*(4), 759-773.e8. https://doi.org/10.1016/j.neuron.2017.04.043

Bosco, D. B., Zheng, J., Xu, Z., Peng, J., Eyo, U. B., Tang, K., Yan, C., Huang, J., Feng, L., Wu, G., Richardson, J. R., Wang, H., & Wu, L.-J. (2018). RNAseq analysis of hippocampal microglia after kainic acid-induced seizures. *Molecular Brain*, *11*(1), 34. https://doi.org/10.1186/s13041-018-0376-5

Boucsein, C., Kettenmann, H., & Nolte, C. (2000). Electrophysiological properties of microglial cells in normal and pathologic rat brain slices. *European Journal of Neuroscience*, *12*(6), 2049–2058. https://doi.org/10.1046/j.1460-9568.2000.00100.x

Boucsein, C., Zacharias, R., Färber, K., Pavlovic, S., Hanisch, U.-K., & Kettenmann, H. (2003). Purinergic receptors on microglial cells: Functional expression in acute brain slices and modulation of microglial activation in vitro. *European Journal of Neuroscience*, *17*(11), 2267–2276. https://doi.org/10.1046/j.1460-9568.2003.02663.x

Bourne, J. N., Kirov, S. A., Sorra, K. E., & Harris, K. M. (2007). Warmer preparation of hippocampal slices prevents synapse proliferation that might obscure LTP-related structural plasticity. *Neuropharmacology*, *52*(1), 55–59. https://doi.org/10.1016/j.neuropharm.2006.06.020

Brahma, B., Forman, R. e., Stewart, E. e., Nicholson, C., & Rice, M. e. (2000). Ascorbate Inhibits Edema in Brain Slices. *Journal of Neurochemistry*, *74*(3), 1263–1270. https://doi.org/10.1046/j.1471-4159.2000.741263.x

Butovsky, O., Jedrychowski, M. P., Moore, C. S., Cialic, R., Lanser, A. J., Gabriely, G., Koeglsperger, T., Dake, B., Wu, P. M., Doykan, C. E., Fanek, Z., Liu, L., Chen, Z., Rothstein, J. D., Ransohoff, R. M., Gygi, S. P., Antel, J. P., & Weiner, H. L. (2014). Identification of a unique TGF-β–dependent molecular and functional signature in microglia. *Nature Neuroscience*, *17*(1), 131–143. https://doi.org/10.1038/nn.3599

Chen, Y., Luan, P., Liu, J., Wei, Y., Wu, Z., & Jing, M. (2022). *Spatiotemporally selective ATP events from astrocytes encode injury information and guide sustained microglial response* (p. 2022.06.21.497103). bioRxiv. https://doi.org/10.1101/2022.06.21.497103

Császár, E., Lénárt, N., Cserép, C., Környei, Z., Fekete, R., Pósfai, B., Balázsfi, D., Hangya, B., Schwarcz, A. D., Szabadits, E., Szöllősi, D., Szigeti, K., Máthé, D., West, B. L., Sviatkó, K., Brás, A. R., Mariani, J.-C., Kliewer, A., Lenkei, Z., … Dénes, Á. (2022). Microglia modulate blood flow, neurovascular coupling,

and hypoperfusion via purinergic actions. *Journal of Experimental Medicine*, *219*(3), e20211071. https://doi.org/10.1084/jem.20211071

Cserép, C., Pósfai, B., Lénárt, N., Fekete, R., László, Z. I., Lele, Z., Orsolits, B., Molnár, G., Heindl, S., Schwarcz, A. D., Ujvári, K., Környei, Z., Tóth, K., Szabadits, E., Sperlágh, B., Baranyi, M., Csiba, L., Hortobágyi, T., Maglóczky, Z., … Dénes, Á. (2020). Microglia monitor and protect neuronal function through specialized somatic purinergic junctions. *Science*. https://doi.org/10.1126/science.aax6752

Davalos, D., Grutzendler, J., Yang, G., Kim, J. V., Zuo, Y., Jung, S., Littman, D. R., Dustin, M. L., & Gan, W.-B. (2005). ATP mediates rapid microglial response to local brain injury in vivo. *Nature Neuroscience*, *8*(6), 752–758. https://doi.org/10.1038/nn1472

Davies, D. S., Ma, J., Jegathees, T., & Goldsbury, C. (2017). Microglia show altered morphology and reduced arborization in human brain during aging and Alzheimer's disease. *Brain Pathology*, *27*(6), 795–808. https://doi.org/10.1111/bpa.12456

Dissing-Olesen, L., LeDue, J. M., Rungta, R. L., Hefendehl, J. K., Choi, H. B., & MacVicar, B. A. (2014). Activation of Neuronal NMDA Receptors Triggers Transient ATP-Mediated Microglial Process Outgrowth. *Journal of Neuroscience*, *34*(32), 10511–10527. https://doi.org/10.1523/JNEUROSCI.0405-14.2014

Elmore, M. R. P., Najafi, A. R., Koike, M. A., Dagher, N. N., Spangenberg, E. E., Rice, R. A., Kitazawa, M., Matusow, B., Nguyen, H., West, B. L., & Green, K. N. (2014). Colony-Stimulating Factor 1 Receptor Signaling Is Necessary for Microglia Viability, Unmasking a Microglia Progenitor Cell in the Adult Brain. *Neuron*, *82*(2), 380–397. https://doi.org/10.1016/j.neuron.2014.02.040

Eyo, U. B., Peng, J., Swiatkowski, P., Mukherjee, A., Bispo, A., & Wu, L.-J. (2014). Neuronal Hyperactivity Recruits Microglial Processes via Neuronal NMDA Receptors and Microglial P2Y12 Receptors after Status Epilepticus. *Journal of Neuroscience*, *34*(32), 10528–10540. https://doi.org/10.1523/JNEUROSCI.0416-14.2014

Eyo, U. B., & Wu, L.-J. (2013). Bidirectional Microglia-Neuron Communication in the Healthy Brain. *Neural Plasticity*, *2013*, e456857. https://doi.org/10.1155/2013/456857

Färber, K., & Kettenmann, H. (2005). Physiology of microglial cells. *Brain Research Reviews*, *48*(2), 133–143. https://doi.org/10.1016/j.brainresrev.2004.12.003

Ferando, I., & Mody, I. (2015). In vitro gamma oscillations following partial and complete ablation of δ subunit-containing GABAA receptors from parvalbumin interneurons. *Neuropharmacology*, *88*, 91–98. https://doi.org/10.1016/j.neuropharm.2014.09.010

Gosselin, D., Skola, D., Coufal, N., Holtman, I., Schlachetzki, J., Sajti, E., Jaeger, B., O'Connor, C., Fitzpatrick, C., Pasillas, M., Pena, M., Adair, A., Gonda, D., Levy, M., Ransohoff, R., Gage, F., & Glass, C. (2017). An environment-dependent transcriptional network specifies human microglia identity. *Science (New York, N.Y.)*, *356*. https://doi.org/10.1126/science.aal3222

Gu, N., Eyo, U. B., Murugan, M., Peng, J., Matta, S., Dong, H., & Wu, L.-J. (2016). Microglial P2Y12 receptors regulate microglial activation and surveillance during neuropathic pain. *Brain, Behavior, and Immunity*, *55*, 82–92. https://doi.org/10.1016/j.bbi.2015.11.007

Hájos, N., Ellender, T. J., Zemankovics, R., Mann, E. O., Exley, R., Cragg, S. J., Freund, T. F., & Paulsen, O. (2009). Maintaining network activity in submerged hippocampal slices: Importance of oxygen supply. *European Journal of Neuroscience*, *29*(2), 319–327. https://doi.org/10.1111/j.1460-9568.2008.06577.x

Hájos, N., Karlócai, M. R., Németh, B., Ulbert, I., Monyer, H., Szabó, G., Erdélyi, F., Freund, T. F., & Gulyás, A. I. (2013). Input-output features of anatomically identified CA3 neurons during hippocampal sharp wave/ripple oscillation in vitro. *Journal of Neuroscience*, *33*(28), 11677–11691.

Hájos, N., & Mody, I. (2009). Establishing a physiological environment for visualized in vitro brain slice recordings by increasing oxygen supply and modifying aCSF content. *Journal of Neuroscience Methods*, *183*(2), 107–113.

Han, J., Harris, R. A., & Zhang, X.-M. (2017). An updated assessment of microglia depletion: Current concepts and future directions. *Molecular Brain*, *10*, 25. https://doi.org/10.1186/s13041-017-0307-x

Haynes, S. E., Hollopeter, G., Yang, G., Kurpius, D., Dailey, M. E., Gan, W.-B., & Julius, D. (2006). The P2Y12 receptor regulates microglial activation by extracellular nucleotides. *Nature Neuroscience*, *9*(12), 1512–1519. https://doi.org/10.1038/nn1805

Heindl, S., Gesierich, B., Benakis, C., Llovera, G., Duering, M., & Liesz, A. (2018). Automated Morphological Analysis of Microglia After Stroke. *Frontiers in Cellular Neuroscience*, *12*, 106. https://doi.org/10.3389/fncel.2018.00106

1146 Hellwig, S., Heinrich, A., & Biber, K. (2013). The brain's best friend: Microglial neurotoxicity revisited. *Frontiers*
1147 *in Cellular Neuroscience*, *7*. https://www.frontiersin.org/article/10.3389/fncel.2013.00071
1148 Hickman, S. E., Kingery, N. D., Ohsumi, T. K., Borowsky, M. L., Wang, L., Means, T. K., & El Khoury, J. (2013). The
1149 microglial sensome revealed by direct RNA sequencing. *Nature Neuroscience*, *16*(12), 1896–1905.
1150 https://doi.org/10.1038/nn.3554
1151 Hirbec, H., Rassendren, F., & Audinat, E. (2019). Microglia Reactivity: Heterogeneous Pathological Phenotypes.
1152 In O. Garaschuk & A. Verkhratsky (Eds.), *Microglia: Methods and Protocols* (pp. 41–55). Springer.
1153 https://doi.org/10.1007/978-1-4939-9658-2_4
1154 Holderith, N., Heredi, J., Kis, V., & Nusser, Z. (2020). A High-Resolution Method for Quantitative Molecular
1155 Analysis of Functionally Characterized Individual Synapses. *Cell Reports*, *32*(4), 107968.
1156 https://doi.org/10.1016/j.celrep.2020.107968
1157 Holtman, I. R., Raj, D. D., Miller, J. A., Schaafsma, W., Yin, Z., Brouwer, N., Wes, P. D., Möller, T., Orre, M.,
1158 Kamphuis, W., Hol, E. M., Boddeke, E. W. G. M., & Eggen, B. J. L. (2015). Induction of a common
1159 microglia gene expression signature by aging and neurodegenerative conditions: A co-expression
1160 meta-analysis. *Acta Neuropathologica Communications*, *3*(1), 31. https://doi.org/10.1186/s40478-
1161 015-0203-5
1162 Huchzermeyer, C., Berndt, N., Holzhütter, H.-G., & Kann, O. (2013). Oxygen Consumption Rates during Three
1163 Different Neuronal Activity States in the Hippocampal CA3 Network. *Journal of Cerebral Blood Flow &*
1164 *Metabolism*, *33*(2), 263–271. https://doi.org/10.1038/jcbfm.2012.165
1165 Ikegami, A., Haruwaka, K., & Wake, H. (2019). Microglia: Lifelong modulator of neural circuits. *Neuropathology*,
1166 *39*(3), 173–180. https://doi.org/10.1111/neup.12560
1167 Ivanov, A., & Zilberter, Y. (2011). Critical State of Energy Metabolism in Brain Slices: The Principal Role of
1168 Oxygen Delivery and Energy Substrates in Shaping Neuronal Activity. *Frontiers in Neuroenergetics*, *3*,
1169 9. https://doi.org/10.3389/fnene.2011.00009
1170 Izquierdo, P., Attwell, D., & Madry, C. (2019). Ion Channels and Receptors as Determinants of Microglial
1171 Function. *Trends in Neurosciences*, *42*(4), 278–292. https://doi.org/10.1016/j.tins.2018.12.007
1172 Kato, G., Inada, H., Wake, H., Akiyoshi, R., Miyamoto, A., Eto, K., Ishikawa, T., Moorhouse, A. J., Strassman, A.
1173 M., & Nabekura, J. (2016). Microglial Contact Prevents Excess Depolarization and Rescues Neurons

from Excitotoxicity. *ENeuro*, *3*(3), ENEURO.0004-16.2016. https://doi.org/10.1523/ENEURO.0004-16.2016

Kettenmann, H., Hanisch, U.-K., Noda, M., & Verkhratsky, A. (2011). Physiology of Microglia. *Physiological Reviews*, *91*(2), 461–553. https://doi.org/10.1152/physrev.00011.2010

Kierdorf, K., & Prinz, M. (2017). Microglia in steady state. *The Journal of Clinical Investigation*, *127*(9), 3201–3209. https://doi.org/10.1172/JCI90602

Kirov, S. A., Sorra, K. E., & Harris, K. M. (1999). Slices Have More Synapses than Perfusion-Fixed Hippocampus from both Young and Mature Rats. *Journal of Neuroscience*, *19*(8), 2876–2886. https://doi.org/10.1523/JNEUROSCI.19-08-02876.1999

Lin, S.-S., Tang, Y., Illes, P., & Verkhratsky, A. (2021). The Safeguarding Microglia: Central Role for P2Y12 Receptors. *Frontiers in Pharmacology*, *11*, 2218. https://doi.org/10.3389/fphar.2020.627760

Liu, Y.-J., Green, K. N., Holmes, T. C., & Xu, X. (2022). Commentary: How Do Microglia Regulate Neural Circuit Connectivity and Activity in the Adult Brain? *Neuroscience Insights*, *17*, 26331055211071124. https://doi.org/10.1177/26331055211071124

Liu, Y.-J., Spangenberg, E. E., Tang, B., Holmes, T. C., Green, K. N., & Xu, X. (2021). Microglia Elimination Increases Neural Circuit Connectivity and Activity in Adult Mouse Cortex. *Journal of Neuroscience*, *41*(6), 1274–1287. https://doi.org/10.1523/JNEUROSCI.2140-20.2020

Madry, C., Arancibia-Cárcamo, I. L., Kyrargyri, V., Chan, V. T. T., Hamilton, N. B., & Attwell, D. (2018). Effects of the ecto-ATPase apyrase on microglial ramification and surveillance reflect cell depolarization, not ATP depletion. *Proceedings of the National Academy of Sciences*, *115*(7), E1608–E1617. https://doi.org/10.1073/pnas.1715354115

Madry, C., Kyrargyri, V., Arancibia-Cárcamo, I. L., Jolivet, R., Kohsaka, S., Bryan, R. M., & Attwell, D. (2018). Microglial Ramification, Surveillance, and Interleukin-1β Release Are Regulated by the Two-Pore Domain K+ Channel THIK-1. *Neuron*, *97*(2), 299-312.e6. https://doi.org/10.1016/j.neuron.2017.12.002

Mann, E. O., Suckling, J. M., Hajos, N., Greenfield, S. A., & Paulsen, O. (2005). Perisomatic Feedback Inhibition Underlies Cholinergically Induced Fast Network Oscillations in the Rat Hippocampus In Vitro. *Neuron*, *45*(1), 105–117. https://doi.org/10.1016/j.neuron.2004.12.016

Masuda, T., Sankowski, R., Staszewski, O., & Prinz, M. (2020). Microglia Heterogeneity in the Single-Cell Era. *Cell Reports*, *30*(5), 1271–1281. https://doi.org/10.1016/j.celrep.2020.01.010

1203 Matyash, M., Zabiegalov, O., Wendt, S., Matyash, V., & Kettenmann, H. (2017). The adenosine generating
1204 enzymes CD39/CD73 control microglial processes ramification in the mouse brain. *PLOS ONE*, *12*(4),
1205 e0175012. https://doi.org/10.1371/journal.pone.0175012
1206 Melief, J., Koning, N., Schuurman, K. G., Van De Garde, M. D. B., Smolders, J., Hoek, R. M., Van Eijk, M.,
1207 Hamann, J., & Huitinga, I. (2012). Phenotyping primary human microglia: Tight regulation of LPS
1208 responsiveness. *Glia*, *60*(10), 1506–1517. https://doi.org/10.1002/glia.22370
1209 Mildner, A., Huang, H., Radke, J., Stenzel, W., & Priller, J. (2017). P2Y12 receptor is expressed on human
1210 microglia under physiological conditions throughout development and is sensitive to
1211 neuroinflammatory diseases. *Glia*, *65*(2), 375–387. https://doi.org/10.1002/glia.23097
1212 Miyamoto, A., Wake, H., Ishikawa, A. W., Eto, K., Shibata, K., Murakoshi, H., Koizumi, S., Moorhouse, A. J.,
1213 Yoshimura, Y., & Nabekura, J. (2016). Microglia contact induces synapse formation in developing
1214 somatosensory cortex. *Nature Communications*, *7*(1), 12540. https://doi.org/10.1038/ncomms12540
1215 Miyamoto, A., Wake, H., Moorhouse, A., & Nabekura, J. (2013). Microglia and synapse interactions: Fine tuning
1216 neural circuits and candidate molecules. *Frontiers in Cellular Neuroscience*, *7*, 70.
1217 https://doi.org/10.3389/fncel.2013.00070
1218 Morrison, H. W., & Filosa, J. A. (2013). A quantitative spatiotemporal analysis of microglia morphology during
1219 ischemic stroke and reperfusion. *Journal of Neuroinflammation*, *10*(1), 782.
1220 https://doi.org/10.1186/1742-2094-10-4
1221 Mulkey, D. K., Henderson, R. A., Olson, J. E., Putnam, R. W., & Dean, J. B. (2001). Oxygen measurements in
1222 brain stem slices exposed to normobaric hyperoxia and hyperbaric oxygen. *Journal of Applied*
1223 *Physiology*, *90*(5), 1887–1899. https://doi.org/10.1152/jappl.2001.90.5.1887
1224 Nasu-Tada, K., Koizumi, S., & Inoue, K. (2005). Involvement of β1 integrin in microglial chemotaxis and
1225 proliferation on fibronectin: Different regulations by ADP through PKA. *Glia*, *52*(2), 98–107.
1226 https://doi.org/10.1002/glia.20224
1227 Nimmerjahn, A., Kirchhoff, F., & Helmchen, F. (2005). Resting Microglial Cells Are Highly Dynamic Surveillants
1228 of Brain Parenchyma in Vivo. *Science*. https://doi.org/10.1126/science.1110647
1229 Pannasch, U., & Rouach, N. (2013). Emerging role for astroglial networks in information processing: From
1230 synapse to behavior. *Trends in Neurosciences*, *36*(7), 405–417.
1231 https://doi.org/10.1016/j.tins.2013.04.004

1232 Peng, J., Liu, Y., Umpierre, A. D., Xie, M., Tian, D.-S., Richardson, J. R., & Wu, L.-J. (2019). Microglial P2Y12
1233 receptor regulates ventral hippocampal CA1 neuronal excitability and innate fear in mice. *Molecular*
1234 *Brain*, *12*(1), 71. https://doi.org/10.1186/s13041-019-0492-x
1235 Perumal, M. B., Latimer, B., Xu, L., Stratton, P., Nair, S., & Sah, P. (2021). Microcircuit mechanisms for the
1236 generation of sharp-wave ripples in the basolateral amygdala: A role for chandelier interneurons. *Cell*
1237 *Reports*, *35*(6), 109106. https://doi.org/10.1016/j.celrep.2021.109106
1238 Petersen, M. A., & Dailey, M. E. (2004). Diverse microglial motility behaviors during clearance of dead cells in
1239 hippocampal slices. *Glia*, *46*(2), 195–206. https://doi.org/10.1002/glia.10362
1240 Prinz, M., Jung, S., & Priller, J. (2019). Microglia Biology: One Century of Evolving Concepts. *Cell*, *179*(2), 292–
1241 311. https://doi.org/10.1016/j.cell.2019.08.053
1242 Remy, S., Gabriel, S., Urban, B. W., Dietrich, D., Lehmann, T. N., Elger, C. E., Heinemann, U., & Beck, H. (2003).
1243 A novel mechanism underlying drug resistance in chronic epilepsy. *Annals of Neurology*, *53*(4), 469–
1244 479. https://doi.org/10.1002/ana.10473
1245 Richerson, G. B., & Messer, C. (1995). Effect of composition of experimental solutions on neuronal survival
1246 during rat brain slicing. *Experimental Neurology*, *131*(1), 133–143. https://doi.org/10.1016/0014-
1247 4886(95)90015-2
1248 Sadler, R., Cramer, J. V., Heindl, S., Kostidis, S., Betz, D., Zuurbier, K. R., Northoff, B. H., Heijink, M., Goldberg,
1249 M. P., Plautz, E. J., Roth, S., Malik, R., Dichgans, M., Holdt, L. M., Benakis, C., Giera, M., Stowe, A. M., &
1250 Liesz, A. (2020). Short-Chain Fatty Acids Improve Poststroke Recovery via Immunological Mechanisms.
1251 *Journal of Neuroscience*, *40*(5), 1162–1173. https://doi.org/10.1523/JNEUROSCI.1359-19.2019
1252 Salter, M. W., & Stevens, B. (2017). Microglia emerge as central players in brain disease. *Nature Medicine*,
1253 *23*(9), 1018–1027. https://doi.org/10.1038/nm.4397
1254 Schafer, D. P., Lehrman, E. K., & Stevens, B. (2013). The “quad-partite” synapse: Microglia-synapse interactions
1255 in the developing and mature CNS. *Glia*, *61*(1), 24–36. https://doi.org/10.1002/glia.22389
1256 Schilling, T., & Eder, C. (2007a). Ion channel expression in resting and activated microglia of hippocampal slices
1257 from juvenile mice. *Brain Research*, *1186*, 21–28. https://doi.org/10.1016/j.brainres.2007.10.027
1258 Schilling, T., & Eder, C. (2007b). Ion channel expression in resting and activated microglia of hippocampal slices
1259 from juvenile mice. *Brain Research*, *1186*, 21–28. https://doi.org/10.1016/j.brainres.2007.10.027

Schilling, T., Quandt, F. N., Cherny, V. V., Zhou, W., Heinemann, U., Decoursey, T. E., & Eder, C. (2000). Upregulation of Kv1.3 K+ channels in microglia deactivated by TGF-β. *American Journal of Physiology-Cell Physiology*, *279*(4), C1123–C1134. https://doi.org/10.1152/ajpcell.2000.279.4.C1123

Schlingloff, D., Káli, S., Freund, T. F., Hájos, N., & Gulyás, A. I. (2014). Mechanisms of sharp wave initiation and ripple generation. *Journal of Neuroscience*, *34*(34), 11385–11398.

Schmid, C. D., Melchior, B., Masek, K., Puntambekar, S. S., Danielson, P. E., Lo, D. D., Gregor Sutcliffe, J., & Carson, M. J. (2009). Differential gene expression in LPS/IFNγ activated microglia and macrophages: In vitro versus in vivo. *Journal of Neurochemistry*, *109*(s1), 117–125. https://doi.org/10.1111/j.1471-4159.2009.05984.x

Singh, V., Sadler, R., Heindl, S., Llovera, G., Roth, S., Benakis, C., & Liesz, A. (2018). The gut microbiome primes a cerebroprotective immune response after stroke. *Journal of Cerebral Blood Flow & Metabolism*, *38*(8), 1293–1298. https://doi.org/10.1177/0271678X18780130

Sipe, G. O., Lowery, Tremblay, M.-È., Kelly, E. A., Lamantia, C. E., & Majewska, A. K. (2016). Microglial P2Y12 is necessary for synaptic plasticity in mouse visual cortex. *Nature Communications*, *7*(1), 10905. https://doi.org/10.1038/ncomms10905

Song, W. M., & Colonna, M. (2018). Chapter One—The Microglial Response to Neurodegenerative Disease. In F. Alt (Ed.), *Advances in Immunology* (Vol. 139, pp. 1–50). Academic Press. https://doi.org/10.1016/bs.ai.2018.04.002

Stence, N., Waite, M., & Dailey, M. E. (2001). Dynamics of microglial activation: A confocal time-lapse analysis in hippocampal slices. *Glia*, *33*(3), 256–266. https://doi.org/10.1002/1098-1136(200103)33:3<256::AID-GLIA1024>3.0.CO;2-J

Strackeljan, L., Baczynska, E., Cangalaya, C., Baidoe-Ansah, D., Wlodarczyk, J., Kaushik, R., & Dityatev, A. (2021). Microglia Depletion-Induced Remodeling of Extracellular Matrix and Excitatory Synapses in the Hippocampus of Adult Mice. *Cells*, *10*(8), Article 8. https://doi.org/10.3390/cells10081862

Swiatkowski, P., Murugan, M., Eyo, U. B., Wang, Y., Rangaraju, S., Oh, S. B., & Wu, L.-J. (2016). Activation of microglial P2Y12 receptor is required for outward potassium currents in response to neuronal injury. *Neuroscience*, *318*, 22–33. https://doi.org/10.1016/j.neuroscience.2016.01.008

Thion, M. S., Ginhoux, F., & Garel, S. (2018). Microglia and early brain development: An intimate journey. *Science (New York, N.Y.)*, *362*(6411), 185–189. https://doi.org/10.1126/science.aat0474

Ting, J. T., Daigle, T. L., Chen, Q., & Feng, G. (2014). Acute Brain Slice Methods for Adult and Aging Animals: Application of Targeted Patch Clamp Analysis and Optogenetics. In M. Martina & S. Taverna (Eds.), *Patch-Clamp Methods and Protocols* (pp. 221–242). Springer. https://doi.org/10.1007/978-1-4939-1096-0_14

Trivino-Paredes, J. S., Nahirney, P. C., Pinar, C., Grandes, P., & Christie, B. R. (2019). Acute slice preparation for electrophysiology increases spine numbers equivalently in the male and female juvenile hippocampus: A DiI labeling study. *Journal of Neurophysiology*, *122*(3), 958–969. https://doi.org/10.1152/jn.00332.2019

Verkhratsky, A., & Nedergaard, M. (2018). Physiology of Astroglia. *Physiological Reviews*, *98*(1), 239–389. https://doi.org/10.1152/physrev.00042.2016

Wake, H., Moorhouse, A. J., Jinno, S., Kohsaka, S., & Nabekura, J. (2009). Resting Microglia Directly Monitor the Functional State of Synapses In Vivo and Determine the Fate of Ischemic Terminals. *Journal of Neuroscience*, *29*(13), 3974–3980. https://doi.org/10.1523/JNEUROSCI.4363-08.2009

Wang, S., & Colonna, M. (2019). Microglia in Alzheimer's disease: A target for immunotherapy. *Journal of Leukocyte Biology*, *106*(1), 219–227. https://doi.org/10.1002/JLB.MR0818-319R

Weinhard, L., di Bartolomei, G., Bolasco, G., Machado, P., Schieber, N. L., Neniskyte, U., Exiga, M., Vadisiute, A., Raggioli, A., Schertel, A., Schwab, Y., & Gross, C. T. (2018). Microglia remodel synapses by presynaptic trogocytosis and spine head filopodia induction. *Nature Communications*, *9*(1), Article 1. https://doi.org/10.1038/s41467-018-03566-5

Wu, C., Luk, W. P., Gillis, J., Skinner, F., & Zhang, L. (2005). Size Does Matter: Generation of Intrinsic Network Rhythms in Thick Mouse Hippocampal Slices. *Journal of Neurophysiology*, *93*(4), 2302–2317. https://doi.org/10.1152/jn.00806.2004

Wu, Y., Dissing-Olesen, L., MacVicar, B. A., & Stevens, B. (2015). Microglia: Dynamic Mediators of Synapse Development and Plasticity. *Trends in Immunology*, *36*(10), 605–613. https://doi.org/10.1016/j.it.2015.08.008

Wu, Z., He, K., Chen, Y., Li, H., Pan, S., Li, B., Liu, T., Xi, F., Deng, F., Wang, H., Du, J., Jing, M., & Li, Y. (2022). A sensitive GRAB sensor for detecting extracellular ATP in vitro and in vivo. *Neuron*, *110*(5), 770-782.e5. https://doi.org/10.1016/j.neuron.2021.11.027

Yamamoto, C., & McIlwain, H. (1966). Electrical Activities in Thin Sections from the Mammalian Brain Maintained in Chemically-Defined Media in Vitro. *Journal of Neurochemistry*, *13*(12), 1333–1343. https://doi.org/10.1111/j.1471-4159.1966.tb04296.x

Zrzavy, T., Hametner, S., Wimmer, I., Butovsky, O., Weiner, H. L., & Lassmann, H. (2017). Loss of 'homeostatic' microglia and patterns of their activation in active multiple sclerosis. *Brain*, *140*(7), 1900–1913. https://doi.org/10.1093/brain/awx113

Supplementary video captions

Suppl. Video 1. Time lapse XY (upper) and YZ (lower) views (maximum intensity projections) of a CX3CR1$^{+/GFP}$ microglia moving towards the surface (dotted line) in an acute brain slice. The cell body positions are indicated with coloured dots. Note the extensive process outgrowth and cell body translocation. Scale bar: 10um.

Suppl. Video 2. Time lapse volume view (from YZ view) of a CX3CR1$^{+/GFP}$ microglia with almost stationery cell body, showing still strong process redistribution in an acute brain slice.

Suppl. Video 3. Morphological changes of individual microglia cells within acute brain slices depicted by maximum intensity projections of XY views. The video starts 1h after slice preparation. Scale bar: 10um.

Suppl. Video 4. Morphological differences of individual microglial cells at different timepoints during incubation within acute brain slices depicted by 3D reconstructions via morphological analysis tool (Heindl et al., 2018).

Suppl. Video 5. ATP dynamics throughout the 5 hours period after slice preparation recorded from layers of the cortex and the hippocampus